TAMPEREEN TEKNILLINEN YLIOPISTO
TAMPERE UNIVERSITY OF TECHNOLOGY

ATENA REZAEI

MULTIMODAL IMAGING OF SILVER NANOCLUSTERS

Master of Science thesis

Examiner: prof. Jari Hyttinen
Examiner and topic approved by the Faculty Council of the Faculty of Computing and Electrical Engineering
on 17th August 2016

ABSTRACT

TAMPERE UNIVERSITY OF TECHNOLOGY
Master's Degree Programme in Electrical Engineering
ATENA REZAEI: Multimodal Imaging of Silver Nanoclusters
Master of Science Thesis, 62 Pages, 8 Appendix pages
May 2017
Major: Biomedical Engineering (Medical physics)
Examiner: Professor Jari Hyttinen
Keywords: X-ray Microtomography, Optical Projection Tomography, Silver nanoclusters, Fluorescent labels, Contrast agent, Biological Imaging

Recent developments in Nanobiotechnology have given rise to a novel brand of fluorescent labels, fluorescent metal nanoclusters, e.g., gold and silver nanoclusters. Generally, high atomic number elements such as silver can attenuate more X-ray and it can be considered as label in X-ray microtomography. Features such as ultra-small size, good biocompatibility, non-toxicity and photo-stability made nanoclusters more attractive as a fluorescent label than conventional fluorophores dye in biological imaging. The core concept of this thesis is to analyze silver nanoclusters as contrast agent by the multimodal imaging approaches of X-ray microtomography (MicroCT) and Optical Projection Tomography (OPT). To estimate the absorption and relation of X-ray and fluorescent signal by different concentrations of silver nanoclusters in samples.

AgNCs-Agar with different concentrations of AgNCs, diluted with agar and water and filter paper coated with silver nanoclusters with different dipping time were studied in this work. The imaging implementation divided into three parts: 1. MicroCT imaging of samples (both AgNC-Agar and filter paper), 2. Optical imaging of AgNC-Agar samples by both fluorescent and bright-field modes. 3. MicroCT imaging of samples which were imaged by OPT first.

Afterward, quantitative approach employed to both microCT and optical images to evaluate the relation between X-ray energy and light intensity with different concentrations of AgNCs to assess the amount of X-ray and light absorption by samples. Ideally, higher ratio of AgNCs revealed brighter microCT images due to more X-ray absorption.

In sum, our results showed that the tested silver nanoclusters can be used as a label in both X-ray microtomography and fluorescent OPT since they show contrast in X-ray and optical images. Moreover, depicted graphs demonstrate the linear correlation between data from images of both modalities and different amounts of silver material.

PREFACE

This thesis is the product of several months' research working and true learning experience. It serves as documentation of final part of my master's study.
It was carried out under all the rules and regulations of Tampere University of Technology, department of Electronics and Communications Engineering. The work was implemented at BioMediTech and Computational Biophysics and Imaging Group (CBIG). The project was done in collaboration with Aalto University of Technology, department of Applied Physics.

First and foremost, I would like to express my sincere gratitude to Prof. Jari Hyttinen who instructed me on the project, all the research opportunities, brand new and interesting topic he offered me. I also owe my deep gratefulness to group of people who supervised me during the project, namely, PHD student Kalle Lehto who always encourage me and taught me how to be innovative in research work, all the basic knowledge and trainings on how to work with microCT device and image analysis.

Many thanks to PHD student Ilmari Tamminen who taught me how to think independently, especially in academic work and always persuade me to novel concepts and analytical approaches, always being supportive on chemical knowledge and techniques. I owe my appreciation to PHD student Markus Hannula for sharing his valuable expertise on image processing with me and training on microCT. It worth noting that portion of the thesis implemented in OPT imaging group, therefore, I would like to thank and highlight the contribution of Research Assistant Toni Montonen who took OPT images and helped me to analyze them. Thank you all for always being open to my questions and your constructive feedback and comments. Thanks to Rabin Ras and Isabel Diez from Aalto University of Technology for preparing samples.

My heartfelt thanks belong to Taina and Markku Matis, my Finnish Friend Family, for their all-time care and support here in Finland. I am also grateful for all my friends who accompanied me during tough times.

Last but not least, my deepest love and thank you go to my lovely family for their everlasting love and support. For sure, passing this journey without them was impossible.

Tampere, May 2017
Atena Rezaei

Table of Contents

List of abbreviations and Symbols

c	Speed of Light
e^-	Electron
e^+	Positron
E	Energy of the photon
E_0	Incident Electron
E_{BE}	Binding Energy of Electron
E'	Scattered Energy
$f(x,y)$	Tomographic Image
$g^p(a)$	Ramp Filter
h	Max planck constant
$I_{Bremsstrahlung}$	Intensity of bremsstrahlung
κ	The cone beam angle
$L_z(x',\theta)$	Projection Function
m	Mass of Charge Particle
m_0c^2	Rest Mass of the Electron
N	Transmitted Photon
N_0	Incident Photon
$P^F(\beta,a,b)$	Filtered Projection
$\tilde{P}^F(\beta,a,b)$	Pre-weighted Data
R	Radius
T_-	Kinetic Energy of Electron
T_+	Kinetic Energy of Positron
μ	Linear Attenuation Coefficient
μ_1	Highest Mean Pixel Value
μ_2	Lowest Mean Pixel Value
μCT	X-ray Microtomography
v	Frequency
x	Thickness of the material
Z	Atomic Number
ze	Incident Electron
λ	Wavelength
δ	Dirac Delta Function
γ	The Fan Angle
θ	Angle
2D	Two Dimensional
3D	Three Dimensional
4D	Four Dimensional
Ag NCs	Silver Nanoclusters
Au NCs	Gold Nanoclusters
CBCT	Cone Beam Computed Tomography
CCD	Charge Coupled Detector
CoR	Center of Rotation
CNR	Contrast to Noise Ratio
CT	Computed Tomography
dia	Dialysis

DOF	Depth of Field
ECL	Electrochemiluminescence
EM	Electromagnetic
EtOH	Ethanol
FBP	Filtered Back Projection
FDK	FeldKamp-Davis-Kress
FEP	Fluorinated Ethylene Propylene
FOD	Focus Object Distance
FOV	Field of View
LAC	Linear Attenuation Coefficient
NCs	Nanoclusters
ODD	Object Detector Distance
OPT	Optical Projection Tomography
PMMA	Polymethacrylic Acid
PVE	Partial Volume Effect
PSF	Point Spread Function
ROI	Region of Interest
SD_1	Standard Deviation of Highest Value
SD_2	Standard Deviation of Lowest Value
SDD	Source Detector Distance
sig_f	Signal from Feature
sig_b	Signal from Background
SNR	Signal to Noise Ratio
SOD	Source Object Distance
SR	Synchrotron
THF	Tetrahydrofuran

1.INTRODUCTION

In this work we aim to show for the first time the possibility of the fluorescent silver nanoclusters as contrast agent in multimodal imaging of OPT and X-ray tomography.
We aim to shed new light on the fluorescent silver nanoclusters as an approach for labeling in low contrast tissue in biological imaging. In addition, the purpose of this work is to present microCT images with different contrasts and OPT images of various concentrations of silver nanoclusters samples diluted in agar and water and filter paper coated with silver nanoclusters. To illustrate the usefulness of microCT and OPT for developmental microscopic and optical imaging.

X-ray microtomography (MicroCT) is well-known as a promising image modality which provides 3D imaging of internal structures of object from different angles. The method is non-destructive and non-invasive with high spatial resolution. The technique is feasible for preclinical applications either in vitro imaging meaning analyzing tissue specimen or in vivo imaging of small animals. Although studies have been extended to the shape and number of breast microcalcifications by X-ray MicroCT to evaluate the structural and anatomic features of breast cancer specimen (Willekens et al.2014). MicroCT imaging also offers volumetric images for morphological imaging of embryos and soft tissues (Metscher 2009; Metscher & Muller 2011).
Additionally, microCT allows the precise detection on bone studies, specifically, bone density due to the high signal contrast between bone and soft tissue. Broadly, MicroCT is well suited for investigations on trabecular bone structure and volume (Holdsworth & Thornton 2002).

Another image modality used in the current work is Optical Projection Tomography (OPT) which can be considered as an equivalent of X-ray microtomography whilst OPT is mostly practical for transparent samples. Principally, a high-resolution image will obtain along 400 tomographic projections through 360-degree rotation of sample (Sharpe et al.2002). The technique is equipped with fluorescent mode and bright-field mode. On the other hand, in order to have a comprehensive study, optical projection tomography, in particular, fluorescent imaging is used to estimate the amount of photo-bleaching or light absorption per fluorescent silver nanocluster sample. Although samples are photostable, but they are prone to photo-bleaching.

Recently, there have been extensive studies on metal nanoclusters and particularly a novel class of luminescent metal nanoclusters which play a vital role in applications

such as fluorescent labels for microscopic imaging. In pioneering work by Zheng and Dickson (2002) Au and Ag introduced as strong oscillator strengths and the appropriate alternative for photostable fluorophores due to their features such as being water-soluble, small and extremely bright which are of the paramount importance.

In the primary study by Wu et al. (2010), AuNC appeared as the contrast agent for diagnosis tumor in vivo by near infrared (NIR) fluorescent imaging which AuNCs considered as a low-toxic contrast agent injected in mice. Fluorescent images exhibited a high tumor uptake of AuNCs with significant contrast from the tissues surrounding the tumor. The results of the study introduced the ultrasmall AuNCs as an emerging contrast agent for in vivo fluorescent tumor imaging due to its long-term photo-stability. Recently gold nanoclusters have been used beyond the diagnostic applications for cancer treatment by injecting to the body and removing cancer cells (Lukianova-Hleb et al.2016). Following this, Diez & Ras (2010) discussed of novel AgNCs on applications such as fluorescent labels for microscopic imaging and fluorescent probes in molecular sensing.

In the present work, samples were prepared by Diez & Ras (2011) which are fluorescent, stable silver nanoclusters and aqueous solution (Diez et al.2009). To this aim clusters were prepared by reduction of silver ions as well as required scaffold such as polymers (methacrylic acid, PMAA) to avoid the aggregation of silver clusters to larger nanoparticles (Diez & Ras 2010). Totally, 27 silver nanoclusters samples have been studied in this thesis including 18 silver Nanocluster-Agar in tubes with different concentrations of silver nanoclusters in dilution of different amounts of agar and water, the rest of the samples including 9 filter papers coated with silver nanoclusters in different dipping time.

AgNC-Agar samples were imaged by fluorescent mode of OPT first. After that bright field imaging applied. Next the OPT-imaged samples were imaged by microCT to estimate the absorption of X-ray energy. This study also highlights the possible effect of X-ray and light photon exposure on the optical fluorescence in 3D optical imaging and X-ray attenuation in the nanoparticles. Following this, the thesis explored the relationship between the X-ray and fluorescent signal versus different amounts of silver nanoclusters. Moreover, possible effect of exposure time in fluorescent imaging and X-ray attenuation on optical properties of silver nanoclusters have been analyzed.

Generally, the grayscales in microCT images presents the X-ray attenuation which indicate the proportional amount of absorbed or scattered X-ray by the sample corresponding to its density and composition of material. Therefore, in this thesis we want to show the correlation of X-ray and light absorption in microCT or fluorescent images based on different amounts of silver nanoclusters as contrast agent.

2.THEORETICAL BACKGROUND

2.1. X-ray Imaging

Over the past decades the discovery of X-radiation by Röntgen (1895) (Bushberg et al. 2012), huge developments were obtained by this breakthrough in different fields of researches and studies. Following this, X-ray has been facilitated from medical applications, for radiographic images in clinical diagnosis to patterning the structure of crystals in X-ray crystallography by X-ray diffraction (Smyth & Martin 2000). To date, numerous studies have proved X-ray as a stepping-stone in medical applications such as computed tomography (CT) and in particular, X-ray microtomography (μCT). X-ray computed tomography is considered as a non-invasive and non-destructive approach (Stock 2009). Herein, literature and physics behind the X-ray imaging are provided to familiarize the reader with the principles of X-ray Microtomography, which is the core concept of this thesis.

2.1.1 Physics of X-ray Imaging

X-ray is the form of electromagnetic energy with wavelength from 0.005 to 10 nm approximately. They overreach to gamma rays at short wavelength side and they come to ultraviolet radiations at the long wavelength end (Van Grieken & Markowiczf 2002). X-ray is also known as an ionized radiation, since it has sufficient energy to release a bounded electron from the atomic shell. In this case, an ion pair will form consisting of a negative electron (e^-) and positive charged atom (Beutel et al. 2000).

Figure 1 shows the electromagnetic spectrum and its wavelengths. As can be seen, gamma rays have the shortest wavelength while Microwave has the highest wavelength. The shorter the wavelength is, the higher the energy it carries. The diagram below displays the electromagnetic spectrum and the relation between frequency and energy.

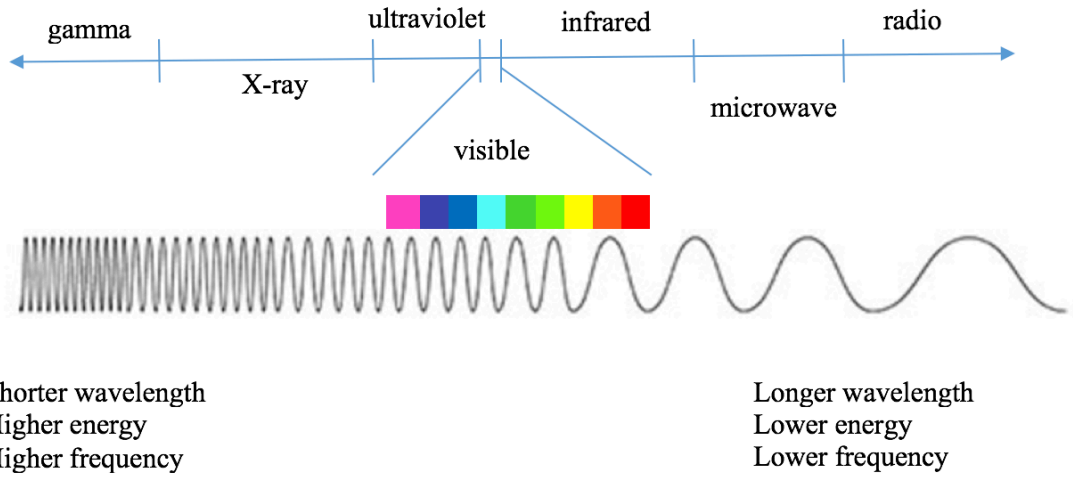

Figure 1. Electromagnetic spectrum. The figure shows the relation between energy and frequency of the wavelength. The spectrum is depicted with some modifications to the original figure by Imagine the Universe, NASA.

The quantum energy per photon can be calculated by:

$$E = h\nu$$

While E stands for Energy of the photon, h = 4.136 X 10^{-18} keV denotes Max Planck constant and ν means Frequency. Moreover, the above formula in the extent of wavelength can be described as:

$$\lambda = \frac{c}{\nu}$$

Therefore,

$$\mathrm{E} = \frac{hc}{\lambda}$$

Which c = 2.998 x 10^8 m/s is the speed of light and λ stands for wavelength (Attix 1986).

Since electromagnetic spectrum consists of different levels of wavelength, energy of each wave can be calculated based on particular wavelength.
Adding to this, electromagnetic waves are characterized by wave-particles dual nature. The concept explains that light behaves both as wave and particles or quanta of energy like a photon. This concept is more acceptable in small scale components (Bushberg et al.2012). Photoelectric effect and Compton scattering consider as particles properties of light and X-ray scattering supports wave behavior of radiation (Morrison 2010). It is beyond the scope of this thesis to provide comprehensive information about the wave-particle duality concept. However, photoelectric effect and Compton scattering will be explained further in 2.1.3 section.

2.1.2 X-ray Production

Bremsstrahlung X-ray

Bremsstrahlung radiation or braking radiation is a phenomenon, which occurs in X-ray Tube. Basically, the X-ray tube is in a vacuum, otherwise, high-speed electrons may strike to air molecules and lose their energy. The tube consists of main elements such as, the cathode filament and anode target, stator and lead shielding. When charged particles decelerate, they will produce electromagnetic energy. X-ray electrons from cathode are accelerated by high voltage (40 to 150 kV for general diagnostic X-ray imaging) and strike to anode target, which is made of Tungsten.

Tungsten opted as the suitable metal due to its high atomic number (Z=74) and its high melting point (3300 $°C$) (Beutel et al.2000). Moreover, a large portion of electrons can be turned to X-rays by high atomic target than lower one. After the collision of energetic electrons to the anode, electrons will decelerate and release their energy as Bremsstrahlung X-ray. Rest and most of the energy are converted to heat since most of the electrons lose their kinetic energy by multiple collisions and the small amount of energy release as fluorescence X-rays. Heating in the vacuum might cause a problem, so cooling the system is required. To this aim, anode is rotating to make the tube cool down (Attix 1986). Figure 2 demonstrates the X-ray tube and its major components.

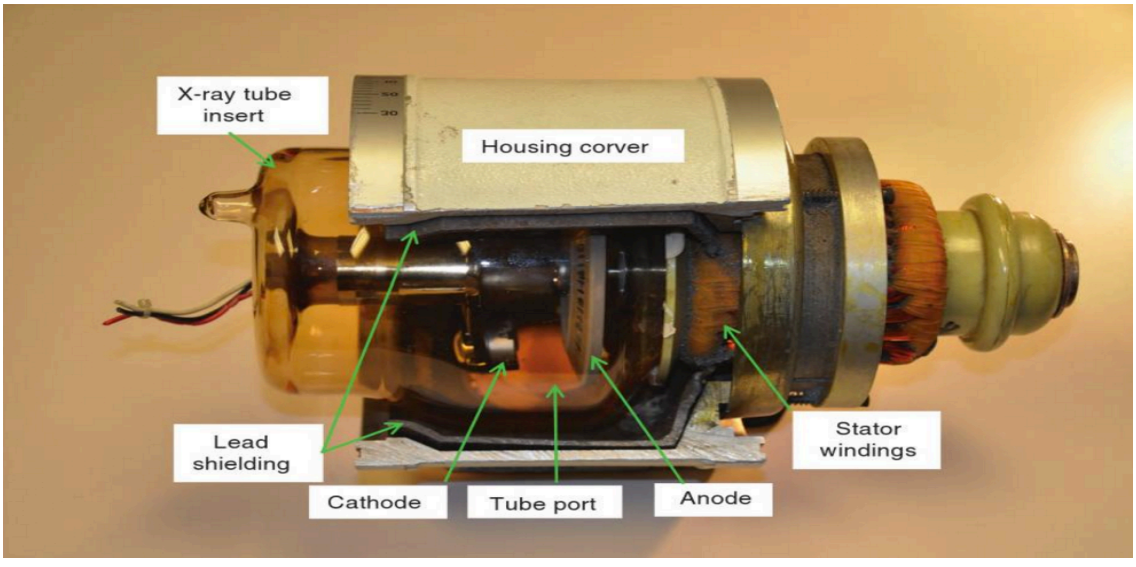

Figure 2. Diagram of X-ray tube, shielding thickness considers as 2mm (Bushberg 2012)

The intensity of bremsstrahlung can be described as:

$$I_{Bremsstrahlung} \propto \frac{Z^2 z^4 e^6}{m^2}$$

Where Z refers to atomic number of the target, m mass of the charged particle and ze indicates the incident electron toward the nucleus.

In terms of the atom and considering the nucleus as a target when an incident electron hits the nucleolus it loses its kinetic energy (deceleration) and produces X-ray. It depends on the distance of projectile electron and striking of the nucleus. If the electron hits the nucleus directly a large amount of energy will be generated. On the contrary, if the electron hits the adjacent area no more energy than the first direction will produce. Figure 3 illustrates the amount of X-ray energy based on the distance of the incident electron (Beutel et al.2000).

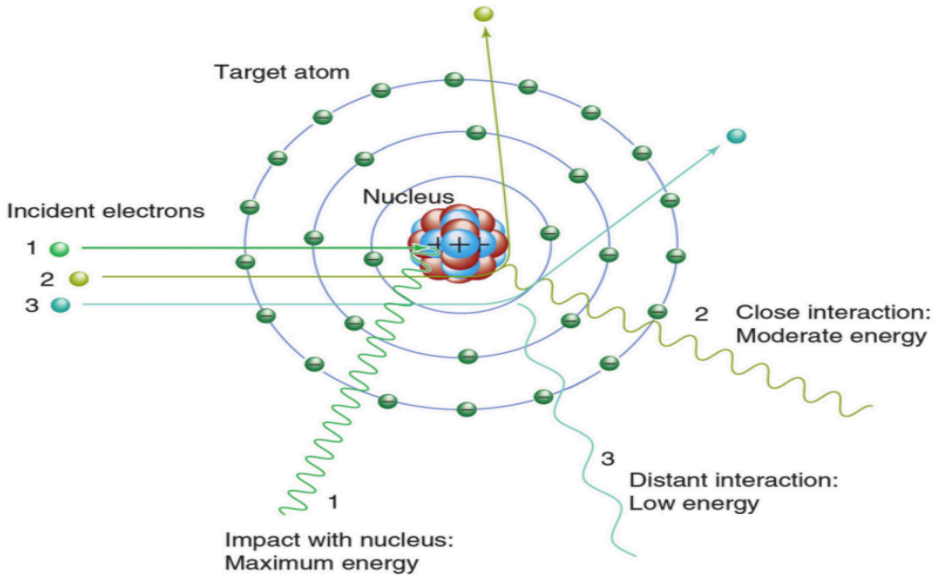

Figure 3. Bremsstrahlung radiation. Three types of X-ray production based on the distance of projectile electron and target. The first incident electron generates higher energy since it directly hits the nucleus. Second electron interacts closer to nucleus and produces less energy while third incident electro strike the shell and emits much lower x-ray (Bushberg et al.2012)

2.1.3 X-ray Interactions

This section will discuss the four major interactions of X-ray with matter. When X-ray interacts with matter, it will be either absorbed, scattered or traverse the material without any interaction. Als-Nielsen claims that the process of these interactions can

shed light on further information of matters and unravel the properties and characteristics of the object (Als-Nielsen 2008).

2.1.3.1 The photoelectric Effect

The photoelectric absorption occurs when photon energy hits the matter with high atomic number (Bushberg et al.2012). When object absorbs the X-ray, X-ray photon will knock the electron out from the K-shell, therefore the phenomenon is called photoelectric effect and ejected electron is photoelectron. After that vacancy of photoelectron will be filled with outer shell electron (L-shell). The kinetic energy of photoelectron (T) is equal to the difference between incident electron (E_0) and binding energy of the electron (E_{BE}):

$$\mathrm{T} = E_0 - E_{BE}$$

Since electrons near atom (K-shell) bound tightly, high X-ray energy is required to overcome the binding energy, so it is essential that $E_0 \geq E_{BE}$ to photoelectric effect occurs. Eventually, ejected electron is appeared as single e^- and ionization will occur. Figure 4 shows the photoelectric effect (Beutel et al.2000)

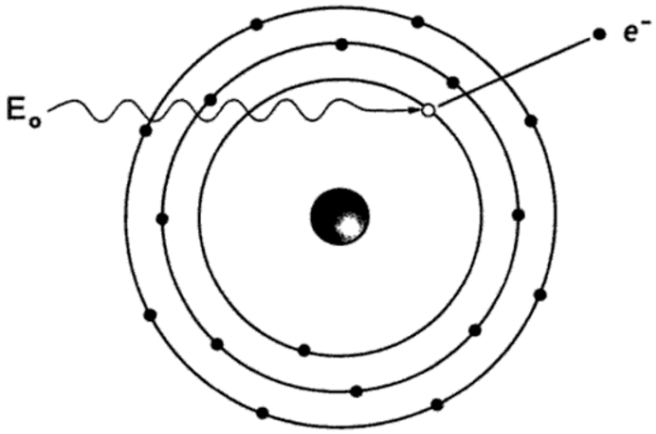

Figure 4. Photoelectric effect. Incident X-ray with E_0 energy interacts with atomic electron and electron from inner shell is liberated. Free electron from the atom is considered as photoelectron (Beutel et al.2000).

2.1.3.2 Compton scattering

Compton scattering or inelastic or incoherent scattering is a proper explanation of particle behavior of light. According to the classical theory of light, when X-ray photon with high energy strikes the outer-shell electron of atom, the outcome of collision is scattered photon with much lower energy but longer wavelength and a detached electron

called Compton electron (Figure 5). Both scattered photon and electron will travel at different angles compared to incident photon (Beutel et al.2000). Compton scattering leads to ionization of atom as a matter of ejected single electron, which lost its kinetic energy through excitation (Bushberg et al.2012). After collision, electron will have kinetic energy of T,which is the difference between incident photon E_0 and scattered energy E',

$$T = E_0 - E'$$

the relation between scattered photon with angle θ and how much energy it lost after scattering can be found from:

$$E' = \frac{E_0}{1 + (\frac{E_0}{m_0 c^2})(1 - cos\theta)}$$

Which $m_0 c^2$ is the rest mass of the electron, which notes as 511KeV (Beutel et al.2000). Figure 5 presents the Compton scattering via scattered photon and ejected electron relative to its angle to incident photon, the greater scattering angle is, the smaller is the energy of the leaving photon.

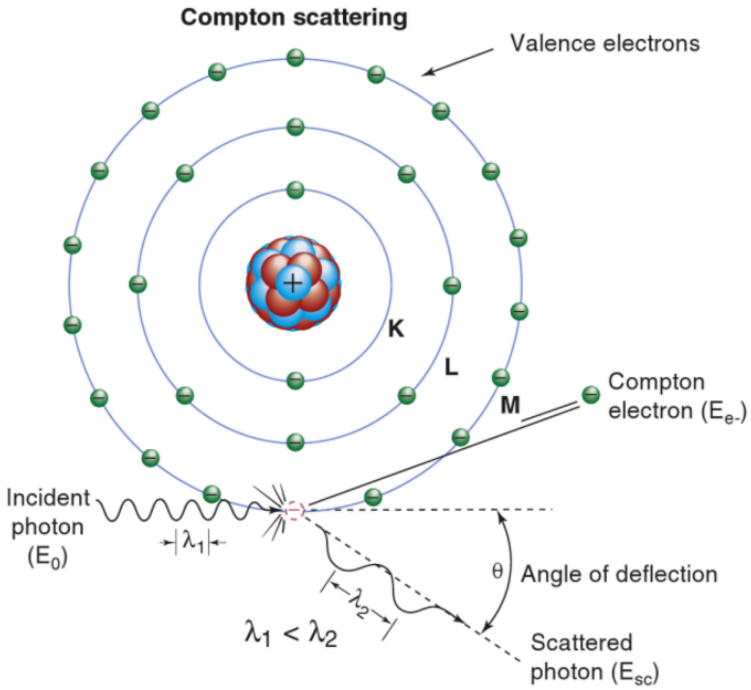

Figure 5. Compton scattering. Incident photon hits the outer-shell electron and produce ejected electron and scattered photon with angle relative to incident photon. Since projectile photon loses much of its energy via scattering the wavelength of scattered photon is longer than incident photon (Bushberg et al.2012).

2.1.3.3 Rayleigh scattering

Rayleigh scattering or classical scattering or coherent scattering occurs when X-ray interacts with atom without losing energy. In this case, photon energy collides with electrical field of orbital electron; this makes vibration of whole electrons in atom and emits scattered photon with the same energy as incident photon ($E' = E_0$). Due to this fact, Rayleigh scattering called elastic event (Attix 1986; Beutel et al.2000; Bushberg et al.2012). One major characteristic that makes the Rayleigh scattering distinguishable from Compton scattering is no that ionization occurs and interaction happens with low photon energy (Beutel et al.2000). Figure 6 illustrates Rayleigh scattering.

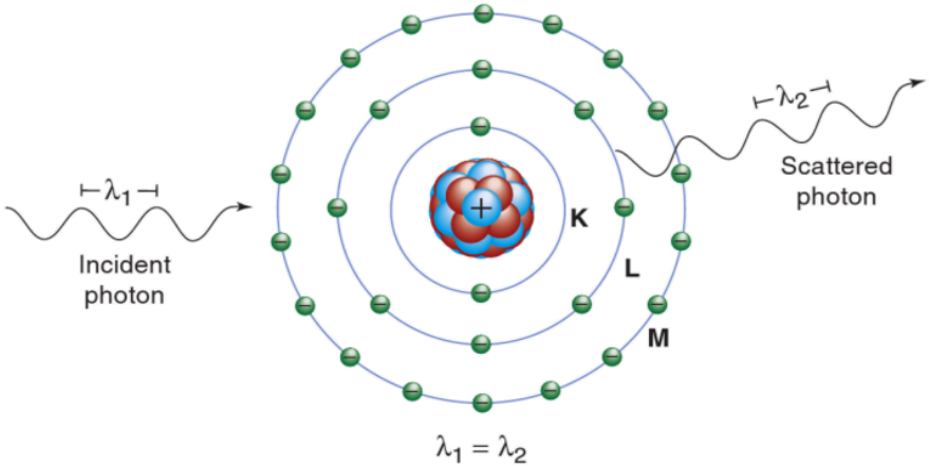

Figure 6. Rayleigh scattering mechanism. An incident photon interacts with the atom and emits a photon with the same energy and wavelength as incident photon (Bushberg et al.2012).

2.1.3.4 Pair production

Pair production will happen when an incident photon interacts with the electric field of atomic nucleus. This interaction will occur only if incident photon has energy above 1.022 MeV, in this case, the photon hits the nucleus and imparts its energy to produce a pair of electron (e^-) and positron (e^+).

$$E_0 = 2m_0c^2 + T_- + T_+$$

In which E_0 stands for total energy of incident photon, $2m_0c^2$ is the rest mass of electron and positron and T_- and T_+ denote kinetic energy of electron and positron, respectively. Figure 7 depicts the pair production interaction (Bushberg et al.2012).

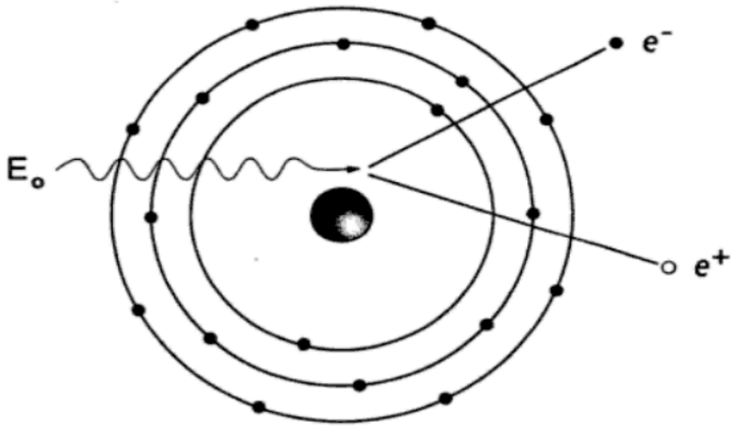

Figure 7. pair production. An incident photon absorbs by electrical field of nucleus and produces pairs of electron (e^-) and positron (e^+) (Beutel et al.2000).

Although many references consider Pair production interaction part of X-ray interaction but it could not encounter in diagnostic process since it requires high energy of 1.02 MeV to occur, which is beyond the range of X-ray energy for Imaging (beutel et al.2000).

2.1.4 X-ray Filtration

Filtration has a great impact on X-ray spectrum, the amount of different photon energies coming out of the X-ray tube should be considered while designing the imaging. Broadly, by the help of X-ray filtration, so-called beam hardening artifact can be removed and in medical imaging radiation dose on patients will decrease. Generally, X-ray tube for diagnostic imaging designed with tungsten (Z=74) target anode and acceleration voltage range between 40 and 150 kV_p. Moreover, X-ray beam might have different energies even at the same kV_p due to calibration of the system, anode angle, the generator waveform and the filtration placed inside and outside the X-ray tube and its chamber (Beutel et al.2000).

The concept of filtration is to remove low photon energy, which cannot penetrate to body. Filtration divides into two main categories: $Inherent\ filtration$ and $Added\ filtration$. The former is made up of glass or metal (aluminum) with a thickness in millimeter and placed into the X-ray tube and attenuate X-ray beam at lower energy. After generating the X-ray beam by tungsten target, it passes through the glass or metal in X-ray tube housing. Inherent filtration also consists of X-ray tube port, mirror for collimation and a layer of oil around X-ray tube for thermal and electrical resistance (Beutel at al.2000). Added filter is inserted in the beam path to absorb photons with low energy. The purpose of Added filter is to absorb so-called ‘’soft

‘’photons with low energy which are incapable of passing through patient and does not provide any useful information of sample and will increase beam hardening and average beam energy because of high attenuation (Attix 1986). Al, aluminum is the most used material in $added$ filter, although plastic and copper are used as well. Hereby, the total filtration is a combination of $inherent$ and $added\ filtreation$, which, narrow the beam spectrum and generate more uniform beam toward the detector (Bushberg et al.2012).

Absorption is common imaging method in conventional medical imaging. In this case, the intensity of beam decreases exponentially as the speed of beam decreases gradually via passing through the material. The absorption coefficient of X-ray beam relatively increases with the atomic number of material. The larger is the atomic number, the greater is absorption and contrast. This fact holds true for the higher density material such as bone that is well visible from other soft tissues. Whereas, low atomic number materials such as soft tissues and polymers required an approach to enhanced the contrast and resolution of images. Phase contrast is the desirable approach to illustrate the fine structures of the material (Landis & Keane 2010).

2.1.5 Attenuation coefficient

As discussed in 2.1.3 section, some of the X-ray photons can be absorbed by the sample like photoelectric effect or occur by Compton scattering. Therefore, it is important to know how much energy, photons will be absorbed or scattered from the material to attenuate the beam. The number of photons are traversing through sample, considerably depends on the atomic number (Z) of material. As an example, soft tissues do not absorb high X-ray energy due to their lower Z and while denser materials such as bone and metal have higher attenuation coefficient.
In particular, linear attenuation coefficient μ represents the fraction of how much incident photon from monoenergetic X-ray passes through the object per thickness x of material in centimeter (cm) and how much X-ray will be attenuated in unite of cm^{-1} . The relation below represents the exponential behavior of transmitted photons N and incident photons N_0 :

$$N = N_0\, e^{-\mu x}$$

Another explanation is possible for attenuation, which is the mass attenuation coefficient. Hence mass attenuation coefficient can be defined as (Bushberg et al.2012):

$$N = N_0\, e^{(-\frac{\mu}{\rho})\rho x}$$

unit μ here is the area per mass which mass attenuation involves with the density of the matter, this can be described by normalization of linear attenuation coefficient and unite

of $\frac{cm^2}{gr}$ (Bushberg et al.2012). The denser the tissue is the more X-ray will be attenuated. For instance, in bone or metal elements X-ray will be more attenuated than soft (lung) tissue. Therefore, in this case, detector will not receive enough photons. Different densities can be useful to describe the X-ray images. For example, low density material such as air represent black spot in images while metal implants show white spots in X-ray images. Other tissues can be considered as different of grayscale depending on their density and thickness.

2.2 Principles of X-ray Microtomography

X-ray micro tomography is conceptually derived from X-ray computed tomography (CT) generation. CT is a medical imaging technique which projections from different angles of patient are obtained to map and visualize the internal structures. The approach is non-destructive and non-invasive. Non-destructive in terms of X-ray can penetrate through the samples and no mechanical dissection is needed. In principle, in computed tomography source and detector rotate around the patient to obtain a series of projections from different angles (Webb 2003).

Primary CT scanners equipped with linear array of photodetector, meaning 3D images obtained and reconstructed one plane by one plane, this is called fan beam CT. Another substitute acquired images in 2D projections. The So-called cone beam CT (CBCT) make the imaging time faster by capturing image of specimen in one rotation (Li et al.2008; Landis & Keane 2010).

Although with the advent of CT scanner, huge evolution occurs in medical imaging field, it carries some restrictions such as, each image represented the structure just in 2D plane of image and structures in region of interest (ROI) and features such as tumors could not be visible clearly out of the 2D plane. Furthermore, each 2D image indicates the average absorption of X-ray by the out-of-field object, which means, the image would not cover all data.

Considering limitations of CT, microcomputed tomography or microCT fulfill the need of 3D image at micron level. Micro Computed tomography is known as high-resolution sibling of medical CT scanners which spatial resolution of image can reach to 1 micrometer (Landis & Keane 2010; Stock 2008). On similar route, recently nanoCT, with spatial resolution below 1 μm, has gained a measure of acceptance for example $in\ vivo$ studies in laboratories (Stock 2008). Further information relevant to nanoCT topic is beyond the scope of this thesis.

MicroCT is considered as both qualitative and quantitative imaging approach. It is qualitative method since it gives this opportunity to researchers to separate the sample into different parts virtually, in other words to segmen the reconstructed volume, regardless of any need for histology even with submicrometer resolution and it brings quantitative analysis of structures both $in\ vivo$ and $in\ vitro$ images based on the absorption of X-ray and 3D reconstruction of microCT data set. For greater depth and breadth, comprehensive studies have been reviewed by Betz et al. (2007) and Holdsworth & Thornton (2002).

3D microtomography images are reconstructed from series of 2D images of each slices where each voxel, of 3D digital image shows the X-ray absorption at specific point. This reveals that each voxel correlates with the mass density of localized tissue. Consequently, comprehensive signal information can be achieved from each voxel (Metscher & Muller 2011). The development of microCT, has enabled to acquire 3D images with high resolution used in non-clinical fields, namely, material science, biological and physical science (Narra et al.2015; Blanquer et al.2017; Stock 2008; Landis & Keane 2010).

Recent studies indicate discernable results of X-ray microtomography (MicroCT) for molecular imaging like morphological imaging of embryos and soft tissues to get quantitative data compared to optical projection tomography (Metscher & Muller 2011).

There are two different basic infrastructures of MicroCTs: in the first structure, source and detector are settled inside the gantry and they move around the sample. In this system source-detector distance (SDD) is predefined by the company maker. However, geometrical magnification relies on the matrix size of the detector and the state of the focusing of X-ray tube source. In the second structure of micro CT source and detector are stationary-oriented and the sample rotates horizontally or vertically along the beam path. In this case source-object distance (SOD) and object-detector distance (ODD) can be set up freely by user which leads to desirable geometrical magnification. However, the object should be in controlled oriented on its own axis to avoid movement blurring. Moreover, small focal spot size of the X-ray tube decreases the penumbral blurring while larger focal spot adds noise to the image (Schambach et al.2010).
X-ray tube of microCT divides into two different categories:

Laboratory X-ray

This type of the tube source is similar to the primary X-ray tubes, that electrons will be accelerated in the electrical field to generate either characteristic X-ray or bremsstrahlung. Laboratory-based X-ray tubes generate microfocus X-rays. In this case, there is no monochromator and X-ray spectrum contains a wide range of energy (Mizutani & Suzuki 2012).

On laboratory scale there are different X-ray detectors such as CCD, flat-panel detector. Generally, in digital X-ray imaging system, the X-ray image will be considered in both spatial and intensity dimensions. Detectors in digital X-ray imaging system such as flat-panel detectors are using the thin film transistors which provide access to digital images with more details and contrast of an image. There are two types of digital flat-panel X-ray detectors:

1. Direct detection which convert the X-ray with a photoconductor to generate electrical charges based on X-ray detection. In this detection, pixels incorporate with a conductive and high voltage bias electrode to pick up the charge and a capacitor to store produced charge.
2. In indirect detection there is phosphor layer is in contact with active matrix array to produce X-rays to light (Ristic 2013).

Another type of camera for detecting X-ray which our microCT device includes is Charged Coupled Device (CCD) that acts as high-density shift register since by manipulating the internal voltages charge, it can be transferred from one capacitor to its neighbor. The device includes the sensor such as photoelectric device to read the produced charged and convert the images into digital signal (MicroXCT-200 and MicroXCT-400 User's Guide 2010). More technical information of CCD of our device can be found in chapter 3.1.1.

Synchrotron X-ray

The second type of the X-ray tube, which brings significant enhancement to imaging area, is synchrotron. They offer higher resolution, large intensities, efficient signal-to-noise ratio (SNR), quantitative reconstructions and more importantly phase contrast imaging. In synchrotron, high-energy and accelerated electrons are propelled into a storage ring. They revolve around the ring with the speed of light roughly to produce bremsstrahlung X-ray. To this aim, electrons should be accelerated in bending magnet with curved sections or insertion device (Betz et al.2007). Contrary to the laboratory X-ray tubes, synchrotrons can produce extremely monochromatic X-rays, which each voxel value can represent the weighted average of LAC per voxel (Mizutani & Suzuki 2012).

Synchrotron microCT systems split into two categories: 1. without lenses and 2. synchrotron systems with absorption. The former with voxel size from 1 to 10 μm. With this in mind, the larger voxel size corresponds to larger diameter of sample. The second type, which is based on parallel beams and no more focusing optics. The voxel size in this type of synchrotron microCT is down to 1-2 μm (Stock 2008).

Typically, detectors in synchrotron microCT machines contain: thin single-crystal phosphors, microscope objective lenses and charge coupled device (CCD). Plenty of the

synchrotron microCTs work with different types of the optical lens to obtain different Fields of View (FOV) and voxel sizes. Another fact about the synchrotron microCT is, as the magnification of optical lenses of the detector increases the voxel size decreases which much smaller voxel size represents the smaller field of view and more data collection times with greater brightness (Stock 2008).

Taken together, there are some merits of Synchrotron X-ray source which outweighs demerits of laboratory tube sources. Relinquishing that synchrotron tubes are costly, in synchrotron sources photons with high-intensity transfer to sample with much lower wavelength. Synchrotron source emits X-ray with high flux with greater spectral brightness (Stock 2008).

2.2.1 CT Artifacts

Artifacts may stem from discrepancies between mathematical modeling in reconstructed image and actual physical modeling (Hsieh 2009). Artifacts in tomographic images could be observed and they might interfere the processing dataset. So far, many algorithms and solutions have been investigated to reduce the artifacts in imaging.
In this section most common and prominent artifacts of tomographic images are discussing.

Noise

There are two prominent sources of noise in reconstructed images. The first one is known as additive noise and derives from electrical noise or round-off errors, meaning the final image is a combination of actual image and the image with noise. The second one is Poisson noise, which the quantity of the possible error is the function of photon counts come out of the object and reach the detector. Therefore, it occurs due to the low amount of the photon numbers (Kak & Slanely 1988).
As the noise increases, soft tissues will have poor contrast while dense materials such as bone could be visualized in an image. Considerably, there is an inverse relation between poisson noise and current. Noise can be compensated by increasing the source current (Schulze et al.2011).

Additionally, for further analysis of features in tomographic image, segmentation is required. Following this as the SNR gets lower, the segmentation and analyzing structures will be restricted. Noise is considered stronger in the center of the material as higher attenuation of X-ray beam passes through the object in middle of that. Noise also strongly relies on resolution. Thus, noise will decrease as the slice thickness increased. Another fact worth mentioning is, optimal SNR is obtained by porous materials compared to solid ones of the same material (Davis & Elliot 2006).

One of the common algorithms for reconstruction of images is FBP which will be discussed in chapter 2.2.2. So that, the projection data will be filtered then filtered data will be back projected. Owning to this fact, limited number of X-ray photons, which are incorrect values will also be back projected and this causes the higher amount of Poisson error. Another proposed method to remove noise is iterative algorithms, statistical model which considers to remove noise on each iteration (Boas & Fleischmann 2012).

Ring Artifact

Ring artifact in tomographic images mostly originates from miscalibrated detector due to beam instabilities. Basically, ring artifact represents as bright or dark rings in the center around the axis of rotation (Boas & Fleischmann 2012; Schulze et al.2011). In a broader sense, if there will be scratch or dust on the screen of scintillator or none linear response of CCD due to dead pixel, it will create so-called sharp rings in reconstructed image. Ring artifact also occurs due to point spread function on detector since incoming beams are diverse and defective beams (Axelsson et al. 2006).

Abu Anas et al (2011) suggests several approaches for removing ring artifact in reconstructed images: sinogram processing and post processing. Since ring artifact is quite similar to stripe artifact in sinogram, therefore in this technique, it is recommended to remove stripes from sinogram image then implement filter back projection algorithm to have a 2-D ring free image. Another alternative in sinogram processing is smoothing the sum curve of sinogram by normalization. Although this method is less satisfied to eliminate intensive sharp rings due to normalization. In accordance with the presented approaches median and mean filtering is used in polar domain post-processing method to remove ring artifact. To this aim, the object will be detached from background then artifact template vector will be removed from each row of the polar image to obtain the correct polar image (Abu Anas et al.2011).

Scattering

Scattering artifact originates from the X-ray photons which deviate from their original path towards detector. Photons will scatter via Compton scattering after interaction with matter. Scattered photons will be captured by detector and this reinforce the scattering signal. It is worth noting that number of scattered photons rely on the atomic number of the sample. Because high atomic number object like metal, bone barium will block more photons and cause more X-ray photons to be scattered. The scattering will be more noticeable if the size of the detector is larger, meaning more scattered photons can strike to it. Both scattering and beam hardening leads to streak artifact in reconstructed images. Scattering can also decrease the contrast of soft-tissue (Boas & Fleischmann 2012; Schulze et al.2011).

Beam Hardening

Beam hardening artifact originates from polychromatic X-ray beam and mostly occurs between two highly attenuated objects. Beam hardening is more prominent in object with high atomic number such as bone and metal. In the other words, photons with low energy will be absorbed by matter swiftly due to photoelectric absorption and be attenuated easily compared to high photon energy (Barret & Keat 2004).

Beam hardening error is a nonlinear function of matter's density and distribution (Meagher et al.1990). In 3D reconstruction, image will be back projected and the result will appear in dark streaks (Barret & Keat 2004). Dark bands or streaks create between two high attenuation objects. The reason behind this matter is; the amount of beam that passes through one of the objects at specific tube position is hardened less than the time when beam passes through both objects at the other positions. In addition, bright streaks can also be visible around the dark streak. So far, various techniques have been argued to remove beam hardening such as using filtration to filter low energy before it goes through patient or using iterative reconstruction algorithm (Barret & Keat 2004).

Metal Artifact

Metal artifact is mostly significant in tomographic images especially the ones with orthopedic implants such as hip prosthesis or dental filling corresponds to high atomic number of metal. Based on the shape and density of the metal object, the artifact appears differently (Hsieh 2009). Metal object can cause beam hardening, scattering, poisson noise artifacts, which beam hardening and scattering produce dark streaks in metal and bright streaks at the adjacent metal area (Boas & Fleischmann 2012).

As mentioned in beam hardening metal object attenuates X-ray beam easily and increasingly compared to soft tissue and bone. Therefore, low amount of X-ray photons strikes to detector panel after passing through the metallic object. Following this, insufficient signal from detector cause metal shadows in raw projection which representing streaks artifact. Furthermore, Non-linear attenuation of X-ray spectrum cause Streaks artifact in beam hardening (Zhang et al.2007). Depending on the reason of metal artifact, there are several methods preventing the artifact. Hsieh (1990) demonstrates a technique to correct metal artifact based on processing the projection acquired from the adjacent area of metal object to improve the bone and soft tissue contrast. On the other hand, Zhang et al (2007) argues the technique based on 3D voxel reconstruction from two projections of two different angles.

Partial Volume Effect

Partial volume effect (PVE) considers as bias result in volumetric images particularly, MicroCT images. It occurs when part of the object interferes into the scanning plane. In

the other words, the PVE mostly happens when the thickness of the sample slice increases (Hsieh 2009). Basically, there are two reasons, which make the PVE in image. The former is, the restricted spatial resolution in image, which causes 3D blurring image. The limited spatial resolution makes part of the signal visible outside of the source. Another reason that makes the PVE happening is image sampling. The second reason mostly considers in PET imaging due to tracer distribution (Soret et al.2007). In order to compensate PVE in medical images, it is recommended to use different thin slices to collect over each other to get the thick slice (Hsieh 2009).

Aliasing

Normally, the intensity distribution of X-ray beam is continuous after interaction with the matter. In order to reconstruct the data, discrete sampling of continuous spectrum is required to visualize the projections in temporal domain.
Based on the Nyquist Sampling theorem, the sampling frequency should be higher than twice the largest frequency that contained in the signal. If this theorem violates, then aliasing error will occur (Hsieh 2009). It is worth mentioning that pixel size of the detector plays a major role in aliasing due to under-sampling (Schulze et al.2011).

Motion Artifact

Motion artifact more likely happens due to the movement of object or misalignment of detector or source. Attention should be paid that sample during the imaging process does not move. Even small movement will decrease the image resolution and causes streak artifact in reconstructed 2D and 3D data set**.**
Motion artifact could also originate from sample movement and shift during imaging at MicroCT (MicroXCT-200 and MicroXCT-400 user's guide 2010). Another important fact that might emerge in reconstructed image due to drifting is ''double edges'' of two parts in the image. This correlates with the first and second 180 degree scanning and happens when scans do not occur simultaneously (Davis & Elliot 2006).

2.2.2 CT Image Reconstruction

As the X-ray photon energy passes through the object, it absorbs the photons in 2D plane of x and y while rotating around z axis with specific angle θ. An arbitrary function $f(x, y)$, which can be explained as a distribution of a certain tissue parameters, creates a projection function $L_z\ (x', \theta)$. Projection function is defined as collection of line of integrals which are perpendicular to x'. The mathematical relation can be noted as (Landis & Keane 2010):

$$L_z(x', \theta) = \int_S f(x, y) ds$$

In order to reconstruct tomographic images $f\ (x, y)$ which is series of projections, radon transform depicts the image to the sinogram which is a collection of parallel projections of an object in specific angle (Hsieh 2009). Sinogram is collection of sinosoidal curves, which refers to projections from different angles. Radon transform can be described as (D'Acunto et al.2014):

$$L_z(x', \theta) \cong R\{f(x, y)\} = \iint_{-\infty}^{\infty} f(x, y)\delta(xcos\theta + ysin\theta - x')\, dxdy$$

where δ is Dirac delta function, $L_z(x', \theta)$ is considered as sinogram because the radon transform of off-center is sinusoid. $f(x, y)$ is function of absorption and x' represents the distance between the line and original coordinates in x and y plane. Figure 8 illustrates the collection of line of integrals which are perpendicular to x'.

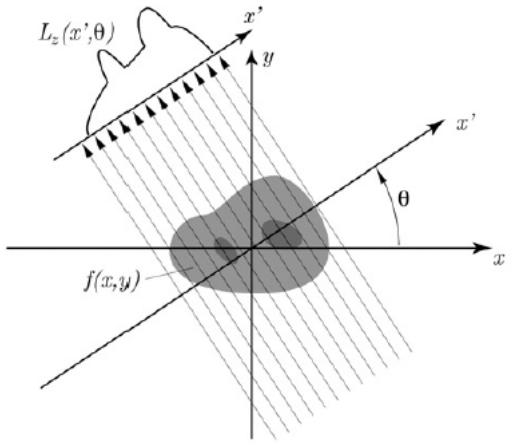

Figure 8. Collection of parallel projections (Landis & Keane 2010)

In order to reconstruct a tomographic image an inverse Radon transform of projection data is required. Toward this end, different algorithms have been proposed, which the most common one used in Micro CT is Filtered Back projection (FBP) (Li et al.2008). Basically, Back Projection converts the measured sinogram to image along the projection lines to the same value in original image. Normally, the image obtained by back projection is blurry. In fact, the FBP technique will filter individual acquisition by convolving each view to kernel filter to remove blurring of back projection. Eventually reconstructed image by FBP is similar to ''correct'' image (Smith 1999).

Another useful algorithm for 3D reconstruction of microCT images is FeldKamp-Davis-Kress (FDK). The approach is quite similar to a 2D FBP algorithm and mostly feasible for Cone-Beam systems. Practically, it is assumed that the data reconstructed by planar detector, $p\ (a, b)$. Figure 9 shows the trajectory source with R radius, projection angle β, the fan angle γ and cone beam angle κ (Li et al.2008).

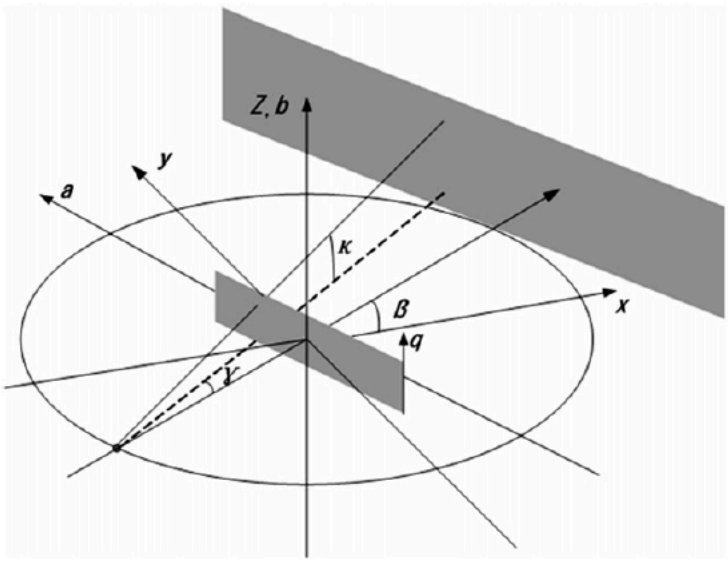

Figure 9. Geometry of FDK with planar detector in plane (a, b) (Li et al.2008)

First each projection will be converted to filter projection $P^F(\beta, a, b)$. Then projection data are pre-weighted and ramp filter convolve with the pre-weighted data:

$$\tilde{P}^F(\beta, a, b) = \left(\frac{R}{\sqrt{R^2 + a^2 + b^2}} . P^F(\beta, a, b)\right) * g^p(a)$$

Where $\frac{R}{\sqrt{R^2+a^2+b^2}}$ demonstrates the cosine of the angle between the X-ray beam of the cone beam when beam strikes to the detector at (a, b) position. The pre-weighted data can be expressed as two parts of fan and cone angle (Scherl et al.2012):

$$\frac{R}{\sqrt{R^2 + a^2 + b^2}} = \frac{R}{\sqrt{R^2 + a^2}} \frac{\sqrt{R^2 + a^2}}{\sqrt{R^2 + a^2 + b^2}} = cos\gamma\ cos\kappa$$

and the last step of the FDK algorithm is back projection of pre-weighted and filtered data to the reconstructed voxel (Li et al.2008):

$$f_{FDK}(x, y, z) = \int_0^{2\pi} \frac{R^2}{U(x, y, \beta)^2} \tilde{P}^F(\beta, a(x, y, \beta), b(x, y, z, \beta)) d\beta$$

where:

$$a(x, y, \beta) = R \frac{-xsin\beta + ycos\beta}{R + xcos\beta + ysin\beta}$$

$$b(x, y, z, \beta) = z \frac{R}{R + xcos\beta + ysin\beta}$$

and:

$$U(x, y, \beta) = R + xcos\beta + ysin\beta$$

2.3 Principles of OPT

Optical Projection Tomography (OPT) is a high-resolution 3D microscopy approach for imaging biological samples (Yang et al. 2015). Compared to microCT, OPT is mostly feasible for transparent samples. The technique is non-destructive and non-invasive, which takes images of specimen up to 15 millimeters thickness (Sharpe et al. 2002). During imaging, sample is rotating 360 degrees around the particular axis while it is located in the transparent tube and immersed in suitable liquid. The device provides two modes of imaging: Fluorescent (emission mode) and Bright field imaging (transmission mode) and the reconstruction of data is processing by Filtered Back Projection (Sharpe et al. 2002; Soto et al. 2016). In case of using OPT for imaging of opaque samples, it is recommended sample be cleaned by benzyl alcohol and benzyl benzoate in order to avoid light scattering. Furthermore, attention should be paid to prevent any drifting during imaging either because of sample movements or apparatus instabilities (Birk et al.2010). Optical projection tomography can provide insights for extensive studies of mapping 3D structure of RNA and embryos (Sharpe et al.2002; Birk et al.2010).

2.3.1 Bright-field Imaging

Optical Projection Tomography is equipped with bright field or transmission mode and emission mode which will be explained in next chapter. In transmission (bright-field) mode white light passes through the sample. The final image forms, based on the light absorption and white light is transmitted through the sample will be collected by lens to form an image. In transmitted OPT, projections reveal the number of photons which travelled across the specimen while they are not attenuating. After acquiring OPT projections, it needs image reconstruction similar as in microCT (Walls et al. 2005).

2.3.2 Fluorescent Imaging

Principally, fluorescent imaging needs target with fluorescent properties. Fluorescence is the emission of light after absorbing light with specific wavelength (e.g. from ultraviolet to infrared) to excite the fluorophores which are the molecules of fluorescent materials. Moreover, part of the excited light might scatter or reflect and part of that absorb during the interaction of fluorophores and photons which at the end fluorophores illuminate light with particular wavelength (Etrych et al.2016).

Furthermore, the difference between the exciting and emitting light is known as the Stokes shift. The energy of the emitted light is lower than absorption light due to vibrational relaxation. Therefore, the emission spectrum of an excited fluorophore has

longer wavelength compared to absorption and excitation spectrum. Generally, larger shifts reveal easier separation of excitation and emission light. Stoke shift is useful property to evaluate how strong fluorescence is and also for building fluorescent microscope (Lichtman & Conchello 2005).

Fluorescent Mechanism

When the fluorophores molecule absorbs sufficient light energy, it causes electronic vibrational or rotational changes in molecule and makes the ‘’ground-state’’ electron (S_0) transition to further orbits of nucleus. In this case electron will be in ‘’excited state’’, S_1. The transition occurs rapidly (in femtoseconds). S_0 represent the energy which is not being excited and respectively S_1 and S_2 are orbits with higher excited energy (Lichtman & Conchello 2005).

According to the $E = h \times c/\lambda$, photon energy E has the indirect relation with wavelength λ and direct link with c, speed of light. To this fact, short wavelength light source (e.g. ultraviolet to infrared) contains higher photon energy to transit the ground state electron to excited singlet state ($S_0\ to\ S_1\ or\ S_2$) (Lichtman & Conchello 2005).

Photo-bleaching phenomenon

Typically, fluorescent dyes are causing the emission of fluorescence. Photo-bleaching or dye photolysis is a phenomenon which fluorescent dyes will be disappeared or decreased within timescale (in this study 3 seconds as an exposure time to activate the fluorophores) due to photochemical alterations of dye. Consequently, this causes degradation and destruction of dyes. Indeed, photo-bleaching has a severe impact on signal-to-noise ratio and diminishes image quality and data during measurement (Pawely James B. 2006). Alternatively, non-covalent interaction of fluorophore and its environmental molecules can cause the fluorescence loss or bleaching. Lichtman & Conchello claim that long-lived triplet state (nonbonding pair electrons in two different orbitals with parallel electron spins) causes the excited electron interacts with other molecules than singlet state (pairs of electron in the same orbital with opposite spins). One crucial criterion makes the bleaching in triplet state is interaction between triplet state fluorophore and oxygen. The outcome of this interaction is chemical reactions which can bleach fluorophores covalently.

2.3.3 OPT Image reconstruction

Filtered back projection (FBP) is known as the useful algorithm to reconstruct both OPT and CT images. Although, Figueiras et al. (2014) proposed the pre-reconstruction

algorithms to get the better reconstructed images by correcting heterogeneous illumination, ring and edge artifact. Moreover, pre-reconstruction algorithms help to detect the center-of-rotation (CoR) in each OPT acquisition. However, many studies have been discussed to calculate the displaced center of rotation without considering primary calibration scans during imaging (Dong et al. 2013). For instance, to reconstruct the same slice many times with distinct offset values and then calculate the total variance of the reconstructed slice to pick the suitable offset value (Walls et al. 2005).

Sometimes reconstructed OPT images appear as blurry images due to defocus images at each projection. In OPT projections, there is a restricted view in objects which it is in the best focus and it called depth of field (DOF). In contrast, objects which are out of the depth of field are considered as out of focus. Since the depth of focus is not always large enough to cover the whole sample, therefore the axis of rotation should be adjusted. Normally, half of the samples at OPT imaging located within depth of field and the other half is outside the depth of field which filtered back-projection reconstruction can process the out of focus data (Walls et al. 2007).

2.3.4 Artifacts

Artifacts can decrease the OPT images' quality. Artifacts in OPT images can be originated from system misalignment, intensity-based signal variations, errors from system or even techniques which applied to remove the artifacts. Insufficient number of angular projections can also degrade the image quality (Chen et al. 2012).

Illumination

OPT imaging needs stable light source to project parallel-rays through the object both in fluorescence or bright-field mode. The former OPT systems were equipped with common source of excited light in fluorescence imaging which was mercury arc gas discharge lamp that covered all wavelengths and full ranges of fluorophores but the lamp provided short and long term fluctuation of the light intensity and proportionally emitted light from fluorescent material. It has been demonstrated that even older mercury lamp makes stronger instability and fluctuation of light but in recent OPT systems, LEDs and lasers are using as source of light (Walls et al.2005).

Additionally, Walles et al. (2005) pointed out that illumination intensity fluctuation can cause bright and dark smears (smear artifact) from reconstructed images due to fluctuated signals. In order to smooth the signal fluctuation, it has been recommended to apply low-pass filter on average fluorescent signal for all projections. Similarly, in bright-field (transmission), measurements represented optimal stability of white light which is transmitted halogen lamp to the diffuser and then specimen (Walls et al.2005).

Signal Decay

Photo-bleaching which discussed in 2.3.2, causes exponential decay of fluorescent signal respect to exposure time. The signal decay can be corrected by normalization of each fluorescent projection. In the other words, considering the fitted exponential curve into average fluorescent intensities then multiplying each projection by suitable normalization constant can reduce the effect of signal decay in each projection (Walls et al.2005).

Streak and Ring Artifact

The average of the CCD response to the photon intensity estimated nonlinear, considering the full dynamic range of CCD. Some dusts on the optical system can also record inaccurate and unreliable data. Due to the nonlinearity of pixels' response, reconstructed images show streak artifact from CCD which is not calibrated properly. This artefact can be visible from the views where the object of high intensity is aligned. Furthermore, concentric rings can be created by different pixel-to-pixel responses. These rings make ring artifact which are along the rotational axis (Walls et al.2005).

Walles et al. (2005) recommends a technique to remove the mentioned artifact. In order to remove the streak artifact CCD needs to be calibrated and in case of preventing ring artifact, pixel-to-pixel variations can be compensated by considering the photon response of every single pixel. In transmitted OPT, streak artifact originates from dark current of CCD and concentric ring artifact create due to variable pixel sensitivity as well as it occurred in emission OPT.

2.4 Image Characteristics

2.4.1 Spatial Resolution

Theoretically, spatial resolution is number of pixel values per unit length. In the other words, spatial resolution makes fine objects visible or defines how well small features can be fitted correspond to reference point (Stock 2009). X-ray images are digital images, which the size of the image defined by pixel. Consequently, an object smaller than pixel size could not be resolved (Bushberg et al.2012). The number of pixels in 2D image plan in different directions (x, y) totally depend on detector configuration (Mizutani & Suzuki 2011). There are several factors that can impact on the spatial resolution of an image such as the size of the X-ray tube focal spot, detector size, system geometry, data-sampling rate and reconstruction algorithm (Hsieh 2009).

Point Spread Function (PSF)

PSF is fundamental concept in measuring resolution of an image. PSF is the response of the system to the input point. PSF is also known as an impulse response function and considered in a 2D image plan of x and y direction, $PSF\ (x, y)$(Bushberg et al.2012).
(Rossman 1969) represents comprehensive explanation of PSF: Point spread function is stated as the intensity distribution in an image of small aperture. In any imaging modality a specific point considers as an input in object plane and output response in the image plane. Point spread function represents the un-sharpness of an image due to optical deficiency. Hence, various input point sources display different intensities. Therefore, output image is sum of the image of each point in the object. Mathematically, it is known as convolution of point spread function multiplied by intensity factor of each point in the object. Point spread function is intensity distributor of the linear and isoplanatic imaging system.

2.4.2 Signal-to-Noise Ratio

The concept of signal to noise ratio in medical imaging is argued to evaluate the amount of background noise proportional to the signal. This noise is originally from the fluctuations of a number of photons which pass through the material then catch by the scintillator and convert to light. Eventually, there is a variation in number of photons that enter detector. Mathematically, Signal-To-Noise ratio SNR is defined as:

$$\text{SNR} = \sqrt{N}$$

Which SNR is equal to standard deviation of N, the number of X-ray photons capture by detector. The purpose is to increase the SNR and amplify the signal.
SNR can be influenced by many reasons. For instance it is proportional to the root square of exposure time and X-ray tube current or the greater is the voltage of X-ray tube ($\text{K}V_p$) more X-ray photons will be produced and this leads to increasing the SNR. Furthermore, the size of the target also impacts on SNR. The thicker is the tissue, the longer path photons should travel and this increases the attenuation meanwhile decrease the SNR (Bushberg et al.2012; Webb 2003).

2.4.3 Contrast-to-Noise Ratio

Contrast is the ratio by the difference of signal between feature and background. In the other words, it is important how to define the object from its adjacent background by considering the lowest and highest intensity (Stock 2009).
Contrast-to-noise ratio or (CNS) has similar definition as SNR. Although, in CNR the image quality is evaluated based on the contrast than signal while in the latter the signal is proportional to background noise of image (Welvaert & Rosseel 2013).
CNR can be mathematically defined as:

$$CNR = \frac{\overline{\mu_2} - \overline{\mu_1}}{\sqrt{{SD_1}^2 + {SD_2}^2}}$$

which μ_1 and μ_2 are highest and lowest mean pixel values from the region of the interest (ROI) and SD_1 and SD_2 are standard deviation values (Michail et al.2015).

2.5 Metal NanoClusters

The silver nanoclusters are in subnanometer size, 2 nm and they show either atomic and nanoparticle behavior or bulk noble metals. According to Fermi wavelength of electrons, nanoclusters (NCs) have discrete energy level. Thus, they show up in different properties such as electrical, optical and chemical.

There are different explanations to represent metal nanoclusters. According to Diez and Ras (2010), metal nanoclusters is described as few-atom metals, which have quantized and discrete energy level and they are of the great interest because nanoclusters link the atomic and nanoparticle behavior in metals.

To date, numerous studies have been conducted to use nanomaterials, notably, metal nanoclusters for fluorescent labeling applications. Much promising metal nanoclusters are rising in fields such as biosensors, molecular imaging, optoelectronic emitters and nanomedicine (Shang et al.2011).

Metal nanoclusters are in small size and good biocompatibility, which make them appropriate enough in different fields such as fluorescent labels for microscopic imaging and fluorescent probes in molecular sensing (Diez et al.2009). Although few studies have investigated on Cu and Pt as metal NCs, recent advances mostly focused on Au and Ag noble metal nanoclusters due to their low toxicity level in biological applications (Shang et al.2011; Wu et al.2010).

Alternatively, gold NCs (AuNCs) could be more promising as a contrast agent for X-ray computed Tomography, which demonstrates desirable and higher X-ray attenuation compared to normal contrast agent, for instance iodine (Zou et al. 2015; Zou et al.

2016). Furthermore, the distinct feature, which makes the gold NCs more suitable for contrast agent in CT images is its long-term stability in blood circulation. This privilege can extend the imaging of tissues or organs (Liu et al.2010).

Additionally, according to recent study of researchers at Rice university, Huston, Texas gold NCs can be used in therapeutic application as well as being diagnostic. New nanotechnology technique is employed to eliminate the cancer cells from tissues. To this end, gold nanoparticles injected to the blood stream. Then gold nanoparticles heated up by short infrared light. This short pulse makes the water inside the molecules vaporized and makes tiny bubbles inside the cancerous cells which leads to expansion and burst and finally ripping the cancer cells apart (Lukianova-Hleb et al.2016).

3.RESEARCH METHODOLOGY AND MATERIALS

Multimodal imaging systems of X-ray microtomography and OPT have been used in this work to image and analyze fluorescent AgNC (Diez & Ras 2011), the samples which prepared by Aalto university of Technology, department of Applied Physics. Section 3.1 provides more information about the imaging device in this study and section 3.2 explain the implementation of the study.

3.1 Research Materials

3.1.1 Imaging Systems

X-ray Microtomography

As mentioned before one of the privileges of the X-ray Microtomography is mapping the internal structures of a sample at high spatial resolution. Xradia MicroXCT - 400 is capable of mapping the internal structure of samples at high spatial resolution. It provides the 3D stack of reconstructed images with resolution down to 1 μm. Furthermore, it can tolerate 15 kg sample in size of 500 mm diameter, 400 mm in height. It includes sample stage which sample could place on that.

Zeiss X-ray Microtomography also contains ergonomic station for further analysis of data and controlling SOD, ODD to get the appropriate geometrical magnification and minimizing penumbral blurring. MicroXCT- 400 is equipped with the shielding door to avoid penetrating ionized X-ray from inside the system to outside. Xradia MicroXCT-400 generates 40 - 150 kilo voltages for producing X-ray (MicroXCT-200 and MicroXCT-400 User's Guide 2010).

Detector assembly of X-ray microtomography includes 6 different lenses in the turret. They include 0.4X (Micro), 1X, 4X, 10X, 20X and 40X, respectively which 4X,10X and 20X consider as standard lenses and 0.4X ,1X and 40X are optional lenses (MicroXCT-200 and MicroXCT- 400 User's Guide 2010) which our device is not equipped with 40X lens. The lenses in X-ray microtomography are similar to optical magnification in conventional microscope for viewing the region of interest (ROI) of sample. Lenses will locate as close as possible to the sample. Care should be taken to

avoid collision when source or detector is moving close to sample. The collision will cause misalignment of sample stage. Lower magnification helps to visualize larger field of view (FOV) of sample. On the other hand, higher magnification depicts smaller Field of view. The sample is rotating 360 degrees to obtain 1600 projections from different angles of sample (MicroXCT- 200 and MicroXCT-400 User's Guide 2010).

The X-ray source of X-Radia MicroXCT- 400 contains beryllium window. Absorption relies on two factors: thickness and mass density of the sample. Absorption goes up as the atomic number of element increases.

In the system set up micro-focal X-ray tube with the anode made by tungsten will produce X-rays and 1k x 1k cooled charge-coupled device (CCD) (Metscher 2009). The detector will capture X-ray photons and digitize them to electrical charges for producing the output image (Li et al.2008). The CCD is utilized with phosphor layer with the fiber optic or optical lens integrated to Thallium-Doped Cesium Iodide scintillator to absorb the incident X-rays photons and convert them to visible light (MicroXCT-200 and MicroXCT- 400 User's Guide 2010). Figure 10 shows the external view of Xradia MicroXCT- 400.

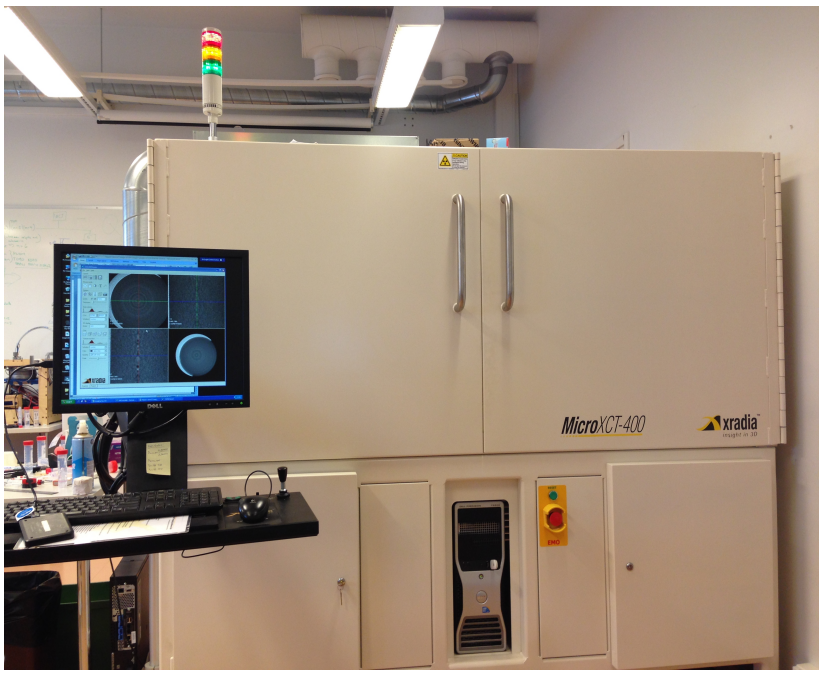

Figure 10. View from outside of the Zeiss MicroXCT- 400 device

The X-ray Microtomography system used in this work is model Zeiss MicroXCT- 400 from Xradia Inc., CA, USA. This scanner is equipped with Hamamatsu L8121-01 Tungsten microfocus X-ray source with an anode voltage between 40-150 kV and output power of 4-10 W with 5 μm focal spot size at 4 W and target current between 0-

500 μA. The Focus to Object Distance (FOD) of the source is 17 mm. This kind of source is specifically used for materials with higher densities.
The X-ray beam is filtered by beryllium window with 200 μm thickness. It is easy to handle the source since it is not tied to the high voltage wiring and the package itself provides air-cooled X-ray source and high voltage power (150kV Microfocus X-ray Source L8121-01 datasheet).It is worthwhile to note that using appropriate source filters will improve the quality of reconstructed image and eliminate low energy X-rays. Furthermore, proper X-ray source voltage will also diminish the beam-hardening artifact.

Z axis is defined as the direction of the X-ray beam path and sample stage movement is limited by 45 mm along the X axis, 100 mm along the Y axis and 50 mm along the Z axis. Detector and source can move toward or away from the sample with limitation distance of 300 mm and 400 mm, respectively. The detector will pick up the X-ray projections to form the image by scintillator, which is integrated into detector. To convert the image into the digital signal. The detector assembly consists of turret which holds up six lenses and CCD camera which is the Andor's iKon-L 936 CCD camera with pixel size 2048 x 2048 (iKon-L _936 Series datasheet). CCD is cooling down to -100° C during the operation to avoid the thermal and dark noise.

In order to analyze data and achieve optimal geometric magnification to adjust source-sample and sample-detector distances, the operating system is mounted on ergonomic station with windows XP and 4GB Ram and 19-inch LCD (MicroXCT-200 and MicroXCT- 400 User's Guide 2010).

Figure 11 shows the source and detector from internal view of MicroXCT- 400.

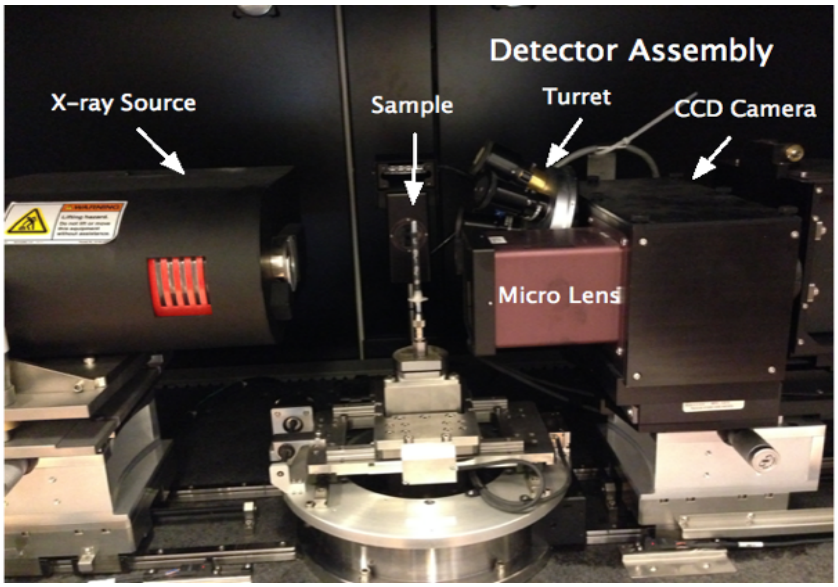

Figure 11. Hamamatsu L8121-01 X-ray source on the left and detector assembly on the right. Micro lense is also visible next to the turret.

MicroXCT- 400 software package consists of XMController, XMReconstructor and XM3DViewer to process tomographic data. The former, XMController manages to control sample from the beginning step to adjust either SOD and ODD for geometrical magnification or optical magnification to data acquisition including acquisition of a projection of a sample at one angle, acquisition of projections of sample through different angles and acquisition of averaged blank images without sample or so-called reference image. Second program XMReconstructor reconstructs the 2D tomographic projection during imaging to 3D stack of the reconstructed image and lastly, XM3DViewer visualizes the reconstructed image to acquire further information of ROI (MicroXCT-200 and MicroXCT-400 User's Guide 2010).

OPT setup

OPT is known as an equivalent of X-ray CT scanning, whereas in OPT, optics makes a focused image on camera (Walls et al. 2005) which in this study 400 images obtained by 360-degree rotation.

Both Fluorescent (Emission) and Bright-field (Transmission) modes of OPT system employed in this work. The bright-field configuration made up of white LED and a telecentric backlight illuminator, Edmund, USA. On the other hand, the fluorescent illumination consists of LED by Thorlabs, USA, and an excitation filter to narrow the spectrum, Edmund, USA. The LED is used for fluorescent illumination has specific wavelength. The wavelength used for fluorescent imaging in this work is 480 nm with excitation filter of 560 nm. It also adjusted by a lens with diffuser (Figueiras et al.2014; Soto et al.2016).

In OPT device specimen are placed in tube made of Fluorinated Ethylene Propylene (FEP) with 1 mm in diameter. The tubes made by Adtech Polymer Engineering, England, and soaked into water inside a transparent cuvette made by Hellma Analytics, Germany. In order to rotate the sample in each orientation, the cuvette is attached to x-y-z motorized linear stage from Standa, Lithuania. AgNCs-Agar tube was located into the cuvette filled with water with refractive index of 1.33. The use of refractive index-matched liquid in imaging helps to reduce the scattering.

In order to detect the light, the system is utilized by 5 X and 10 X long-working distance objective, Edmund, USA, the Numerical Apparatus (NA) of 0.14 and tube lens, Mitutoyo Japan, which can be adjusted by an iris diaphragm, Thorlabs, USA. The final image is captured by CMOS camera, ORCA-Flash 4.0 Hamamatsu, Japan, with 2048 x 2048 pixel array.

Figure 12 displays the general overview of OPT device used in this work.

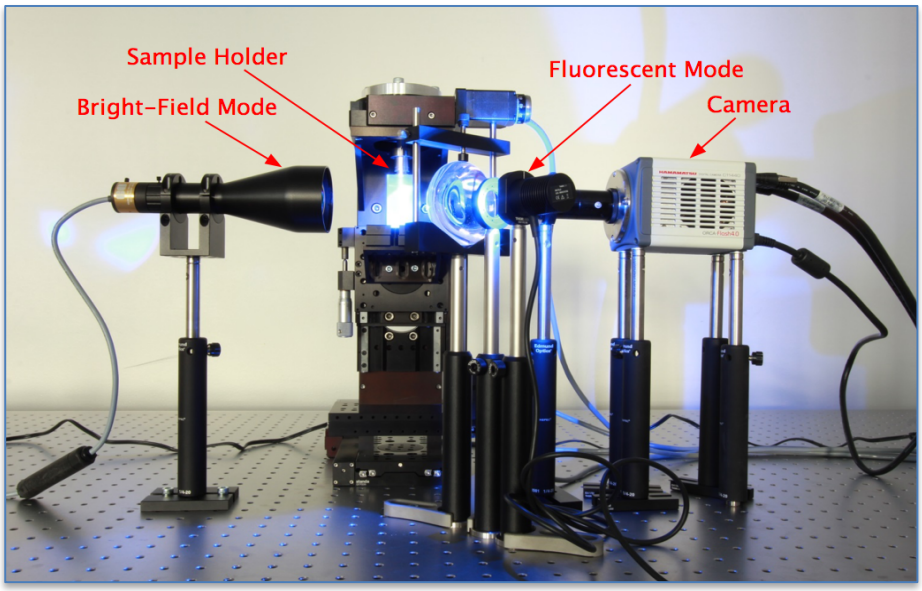

Figure 12. OPT set up

Fluorescent Microscopy; a method in OPT

The fluorescence microscopy has been very demanding during last decade in extent of biology and biomedical science to visualize cells and sub-microscopic cellular components.
Basically, in fluorescence microscopy the labeled specimen is illuminating by excitation source and emitted light gets filtered to obtain the longer wavelength. The most common and well-known of fluorescence microscopy is epi-illumination. In this mode microscope objective lens can magnify the samples or act as condenser lens to orient the light to the sample by passing the excitation light through the microscope objective and use the same objective to capture the emitted fluorescence (Lichtman & Conchello 2005).

The epi-illumination fluorescence microscope has beaten the transmission microscope in a way that, small amount of excited light will be reflected and it is required to be blocked in epi-illumination. Although, both epi-illumination and transmission approaches provide the same amount of excitation of fluorophores (Lichtman & Conchello 2005).

3.1.2 samples

Silver Nanoclusters Preparation

The most distinct feature of current AgNCs used for imaging by OPT and X-ray microtomography in this study is that they are fluorescent and soluble in water (Diez et al.2011).

In Diez's article two types of silver nanoclusters are prepared. T_1 is made of equal volume, 5mg/mL, of freshly prepared aqueous solutions of silver nitrate and PMAA Ag nanoclusters were synthesized at room temperature. After that the solutions exposed to light. The longer exposure time changed the colorless solution to pink the purple. Two sources of light have been used for preparation of nanoclusters: natural day light and desk lamp with fluorescent light source (11W) which both case represent comparable results (Diez et al.2009). Visible light has been used to reduce the impurities of silver nanoparticles from solutions of silver nanoclusters (Diez et al.2009). Optical absorption spectra of the Ag clusters solutions detected from 400 nm to 900 nm by Perkin Elmer Lambda 950 UV/Vis/NIR spectrophotometer (Diez et al.2009).

According to Diez.et al the second type of Ag clusters is made from combination of 200% T_1 cluster solution with specific amount of THF. Then, the purple-colored clustered precipitated during mixing and the precipitation removed from solution and pressed by spatula to remove the absorbed liquid. Lastly, it was rinsed by pure water (Diez et al.2009)

Diez and Ras (2010) claim that during the synthesis of fluorescent silver nanoclusters, different scaffolds namely DNA, proteins, dendrimers and polymers, could be used to make the strong interaction between silver ions and also to prevent clusters, which are in the small size of 1nm into larger nanoparticles. Furthermore, the silver nanoclusters (Ag NCs) samples used in this project work are sustainable in water solutions and contain polymethacrylic acid (PMMA) as stabilizer to form the silver cluster based on their concentration and avoid aggregation (Diez et al.2011).

Remarkably, stabilizers could be PH-dependent of solution (PH$\sim$3) such as PMMA (Diez et al.2009) or temperature-dependent like Dendrimers (Wu et al. 2010). Therefore, the AgNCs sensitive to PH and temperature show responses to any external excitation such as PH and Temperature (Xu & Suslick 2010). For the Ag NCs used in this project, PMMA displays a densely coiled conformation for the formation of Ag nanoclusters.

There are merits and demerits of current AgNCs. For instance, they are bright, photostable, nontoxic and they are in sub-nanometer size while their main drawback is they suffer from photo-bleaching (Diez et al.2011).

The initial set of samples consisted of AgNC-Agar with different concentrations but the same amount of Agar. The silver nanoclusters used for preparation is AgNC 600% with

the molar ratio of Ag:PMAA (polymethacrylic acid) 6:1 which means there are six Ag ions per methacrylic acid unit. So that, AgNCs would be stable for longer time if they stay in dark storage and as a result, there won't be any noticeable changes in precipitation and absorption (Diez et al.2009). Additionally, 100kDa PMAA used as a stabilizer for providing suitable samples, Table 1. Sample AgNC EtOH is extracted with Tetrahydrofuran (THF) and re-dissolved in ethanol in order to remove extra ions. Additionally, AgNC dia sample in agar, dialyzed against water to remove extra free Ag ions. The samples are also included Filter paper (Whatman 1) coated with silver nanoclusters with different dipping time, Table 2.

Further samples (16-27) were provided with different ratios of AgNC and different amounts of Agar and H_2O, Table 3. Second series of samples were prepared as AgNC 600% or AgNC with molar ratio of 1200% (Ag:PMAA 12:1) for further investigations, Table 3 (Information from Aalto University).

Silver nanocluster-Agar in tubes				
Sample	AgNC as	H_2O	Agar	Diluted AgNC, which means decreasing emission intensities
1	0.4 ml	0 ml	0.3 ml	
2	0.2 ml	0.2 ml	0.3 ml	
3	0.1 ml	0.3 ml	0.3 ml	
4	0 ml	0.4 ml	0.3 ml	
				AgNC in ethanol, contains less free silver ions, maybe more stable.
Sample	AgNC EtOH		Agar	
5	0.4 ml		0.3 ml	
				AgNC dialyzed, contains less free silver ions, maybe more stable.
Sample	AgNC dia		Agar	
6	0.4 ml		0.3 ml	

Table 1. Information of preparation the silver nanoclusters-Agar

Filter paper coated with silver nanoclusters			
Sample	Solution	Dipping time	Samples dipped for different periods of time, which means decreasing emission intensities
7	AgNC as	2 h	
8	AgNC as	1 h	
9	AgNC as	30 min	
10	AgNC as	1 min	
			AgNC diluted, which means decreasing emission intensities Here sample 8 fits well too
11	AgNC as dil 1:2	1 h	
12	AgNC as dil 1:4	1 h	
13	H_2O		
			AgNC in ethanol, contains less free silver ions, maybe more stable?
14	AgNC EtOH	1 h	
15	AgNC dia	1 h	AgNC dialyzed, contains less free silver ions, maybe more stable?

Table 2. Information of preparation the filter paper covered with silver nanoclusters

Silver nanocluster-Agar in tubes				
Sample	AgNC 600% as	H_2O	Agar (10mg/ml)	
16	0.025 ml	0.375 ml	0.3 ml	
17	0.05 ml	0.350 ml	0.3 ml	3 mg Agar per sample
18	0.2 ml	0.2 ml	0.3 ml	
19	0.3 ml	0.1 ml	0.3 ml	
20	0.4 ml	0 ml	0.3 ml	
Sample	AgNC 600% as	H_2O	Agar (10 mg/ml)	
21	0.5 ml	0 ml	0.2 ml	2 or 1 mg Agar per sample
22	0.6 ml	0 ml	0.1 ml	
Sample	AgNC 600% as	H_2O	Agar (15 mg/ml)	3 mg Agar per sample
23	0.5 ml	0 ml	0.2 ml	
Sample	AgNC 600% as	H_2O	Agar (30 mg/ml)	3 mg Agar per sample
24	0.6 ml	0 ml	0.1 ml	
Sample	AgNC 600% as	H_2O	Agar	Without Agar
25	0.7 ml	0 ml	0 ml	
Sample	AgNC 1200% as	H_2O	Agar (10 mg/ml)	Highly concentrated AgNC solution!
26	0.1 ml	0.3 ml	0.3 ml	
27	0.4 ml	0 ml	0.3 ml	

Table 3. Information of preparation of silver Nanoclusters-Agar for samples 16-27

3.2 Research Procedure

Image Acquisition

Each sample contained three tubes. To increase the reliability of the measurements and more observations two tubes out of three tubes were imaged by OPT and one tube imaged by microCT. After that, tubes which imaged by OPT imaged by microCT once again. Exceptionally, there were just two tubes for sample 5 of table 1, which one tube was dried (there was no sealed parafilm at one end of the tube). Samples were OPT imaged by an appropriate objective of 10 X and pixel size of 650 nm. For each optical imaging, 400 projections were obtained by every 0.9 degree angle size.
The filter papers (Whatman) coated with silver nanoclusters were not imaged by OPT, since from the preliminary studies of filter paper no signal was detected.

During OPT imaging, in order to get the correct center of rotation for OPT imaging the platform moved by LabVIEW software, National Instruments, USA, and the sample inside the cuvette adjusted manually to locate in the center of field of view.

Firstly, Fluorescent imaging with wavelength of 480 nm utilized and the excitation spectrum was narrowed by 560 nm band pass filter with ± 36 nm as band region cut-off. Secondly, bright field imaging applied. Proper exposure time of 3 seconds and 500 mA as a constant current employed to most of the tubes to activate the fluorescent due to preliminary tests of the present OPT imaging device which proved 3 seconds exposure time and 500 mA constant current are the best match to obtain the optimal results. Alternatively, 1 second exposure time also considered for some tubes and different ranges of exposure time for bright-field mode depend on the best dynamic range. The whole fluorescent imaging took 30-40 minutes long roughly to capture the projections and 10 minutes for bright field Imaging. Table 4 represents parameters which used for OPT imaging of first set of samples Silver Nanocluster-Agar.

OPT Imaging of Silver nanocluster-Agar in tubes				
Sample1	Fluorescent (ExposureTime)	Constant current	Bright Field (ExposureTime)	Magnification
Tube 1	3 s	500 mA	35 ms	10 X
Tube 2	3 s	200 mA	29 ms	10 X
Sample 2				
Tube 1	3 s	500 mA	27 ms	10 X
Tube 2	1s	500 mA	18 ms	10 X
Sample3				

Tube 1	3 s	500 mA	30 ms	10 X
Tube 2	3 s	500 mA	22 ms	10 X
Sample 4	No AgNc			
Tube 1	3 s	500 mA	13 ms	10 X
Tube 2	3 s	500 mA	14 ms	10 X
Sample 5	AgNC EtOH			
Tube 1	3 s	500 mA	28 ms	10 X
Tube 2	1 s	500 mA	28 ms	10 X
Sample6	AgNC dia			
Tube 1	3 s	500 mA	28 ms	10 X
Tube 2	1 s	500 mA	30 ms	10 X

Table 4. parameters used for OPT Imaging of silver Nanoclusters-Agar for samples 1-6

In order to extend the study to achieve reliable and more comprehensive results, samples 16-27 were studied and the process was repeated for the new samples. Table 5 represents descriptive data of OPT imaging of second set of samples (Table 3).

OPT Imaging of Silver nanocluster-Agar in tubes				
Samples	Fluorescent (ExposureTime)	Constant current	Bright Field (ExposureTime)	Magnification
Sample16				
Tube 1	3 s	500 mA	43 ms	10 X
Tube 2	3 s	500 mA	27 ms	10 X
Sample 17				
Tube 1	3 s	500 mA	32 ms	10 X
Tube 2	3 s	500 mA	30 ms	10 X
Sample 18				
Tube 1	3 s	500 mA	28 ms	10 X
Tube 2	3 s	500 mA	23 ms	10 X
Sample 19				
Tube 1	3 s	500 mA	24 ms	10 X
Tube 2	3 s	500 mA	21 ms	10 X
Sample 20				
Tube 1	3 s	500 mA	30 ms	10 X
Tube 2	3 s	500 mA	32 ms	10 X
Sample21				
Tube 1	3 s	500 mA	29 ms	10 X
Tube 2	3 s	500 mA	27 ms	10 X
Sample 22				

Tube 1	3 s	500 mA	26 ms	10 X
Tube 2	3 s	500 mA	29 ms	10 X
Sample 23				
Tube 1	3 s	500 mA	34 ms	10 X
Tube 2	3 s	500 mA	24 ms	10 X
Sample 24				
Tube 1	3 s	500 mA	35 ms	10 X
Tube 2	3 s	500 mA	29 ms	10 X
Sample 25				
Tube 1	3 s	500 mA	39 ms	10 X
Tube 2	3 s	500 mA	21 ms	10 X
Sample 26				
Tube 1	3 s	500 mA	33 ms	10 X
Tube 2	3 s	500 mA	34 ms	10 X
Sample 27				
Tube 1	3 s	500 mA	31 ms	10 X
Tube 2	3 s	500 mA	28 ms	10 X

Table 5. OPT imaging parameters used for samples 16-27 for fluorescent and bright filed Imaging modes

Following the procedure, uCT imaging of samples divided into three parts: 1. uCT imaging of one tube from each sample, 2. uCT imaging of tubes which already imaged by OPT and 3. uCT imaging of filter paper. The same approach continued for the samples of Table 3 which they excluded filter paper.

Sample preparation for microCT imaging

In order to prepare AgNCs-Agar tubes for microCT imaging, three tubes from three different samples were located into a 1 ml in diameter syringe vertically, 1x100 SOFT-JECT (Henke sass Wolf, Germany) and covered by adhesive parafilm on top and enclosed with the piston at the end to be fixed into sample holder. After that, samples were overnight inside the sample platform in microCT to be more stable in terms of the temperature inside the setup and make the drifting as low as possible during imaging. MicroCT imaging of filter paper coated with silver nanoclusters was done separately and the whole stack of filter paper piled and stabled in one syringe to image them at the same time. AgNC-Agar in tube samples were imaged by 20X magnification and voltage of 40 kV. Detector distance and source distance were adjusted to 40 mm and 8mm, respectively.

A pile of filter paper coated with AgNC was imaged by 10 X magnification and 50 kV voltage while detector distance was adjusted to 100 mm and source distance to 10 mm.

more detailed information about the microCT imaging parameters can be found in table A1.1 and A1.2 Appendix 1.

After acquiring X-ray projections, 2D tomographic projections were reconstructed and then visualized to view the 2D and 3D image of each sample. All the reconstructions and visualizations were done by MicroXCT- 400 software programs. Typically, acquisition binning for tomography is 2 and for reconstruction, binning is 1.

Quantitative Approach

In order to show the AgNC as contrast agent, the relation between the light intensity and X-ray attenuation with AgNCs concentration has been analyzed, analysis carried out both on microCT and OPT images to estimate the silver signals and data extracted from images.

A quantitative approach employed to calculate the mean and median to estimate the absorption of X-ray from each reconstructed image. To this aim, each reconstructed image file was opened in XMController program. Then intensity measurement was assessed along the center of each reconstructed image by 400 um line. The central area was considered as the best X-ray absorption area to measure the intensity values. Next, histogram of 400 um line depicted and data of histogram saved as text file then imported into the excel file to calculate the mean and median from each series of data for each image. All measured values (mean and median) were quite close to each other.

Similarly, the same technique implemented on OPT images to extract mean and median values from fluorescent images to evaluate the absorption of light by different amounts of silver nanoclusters. All the values calculated from the fluorescent images with the same exposure time to make the results more comparable. In order to calculate the mean and median, each stack of 400 OPT projections opened by Fiji software (ImageJ). After that each series of values imported in excel. Eventually, mean and median values calculated for each stack.

For interpreting the results, graphs were created to explain the data from MicroCT and OPT images. The former graph represents the bar graphs to analyze the absorption of X-ray or light by samples with the same amount of AgNC but different methods of preparation, the second graph displays correlation between Ag ratio in samples and light or X-ray attenuation and the latter illustrates the behavior of sample during fluorescent imaging. To this point, for each graph linear regression was drawn and R^2 was calculated to evaluate the linearity.

4.RESULTS AND DISCUSSIONS

After imaging the tubes of silver nanoclusters-agar samples turned darker inside due to the light or X-ray absorption except sample 4 and sample 25. One apparent explanation could justify these exceptions is sample 4 considered as a reference image and it did not contain any silver nanocluster while sample 25 does not contain any agar or water to support AgNCs during the fluorescent imaging.

4.1 MicroCT images of AgNCs-Agar tubes and filter paper coated with AgNCs

All the analysis for this study carried out to answer these two questions: 1. what is the best contrast in X-ray microtomography to visualize the silver nanoclusters as a contrast agent and evaluate the possible effect of exposure time on optical properties of samples during fluorescent imaging? and 2. what is the correlation between X-ray and light with the ratio of silver nanoclusters in samples?

With respect to the observations of microCT images of AgNCs-Agar in tubes with pixel size of 1.13 um and filter papers coated with AgNCs, with pixel size of 2.5 um, no fine structures were visible from images to indicate the collective behavior of silver nanoclusters. Adding to this point, general intensity of silver nanoclusters was evaluated by the current magnifications of microCT and no signal of AgNCs was detected to visualize AgNCs since samples are in nano size and quite homogenous.

MicroCT images of AgNCs-Agar in tube demonstrated different levels of grayscale for different amounts of silver nanoclusters in these samples. Figure 13 shows multiple grayscale levels of 2D images of X-ray microtomography.

As can be seen from figure 13, the higher ratio of AgNCs in samples illustrates brighter image, since it absorbs greater X-ray energy to address the attenuated X-ray. MicroCT images of Agar-AgNC provide 2D view of samples in three different fields of view which can be found in appendix 2.

Ring artifact which is the reconstruction error is almost evident in all microCT images due to imperfections of optics. As can be seen from figure 13, there are some noises on images which deteriorated the grayscale. In addition, microCT images of tubes which

first imaged by OPT showed no significant differences with microCT images of samples without OPT imaging. Almost all the MicroCT images of AgNCs-Agar tubes look similar and homogenous.

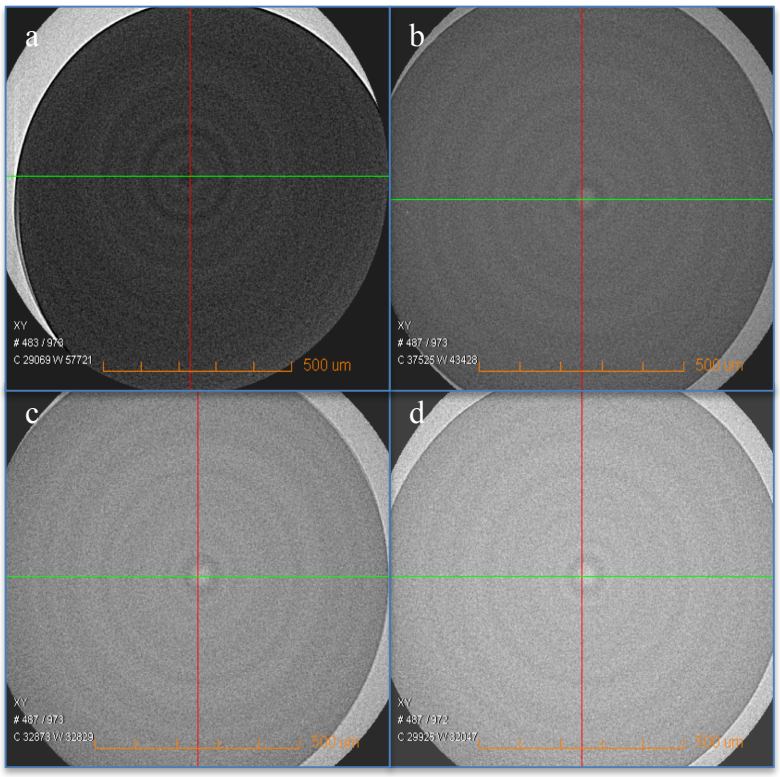

Figure 13. 2D view of different grayscale levels of microCT images for different ratios of AgNCs in samples. a. 0ml AgNCs 600%, b. 0.1ml AgNCs 1200%, c. 0.7ml AgNCs 600% and d. 0.4ml AgNCs 1200%

Figure 14 illustrates the 3D view of Agar-AgNCs by microCT.

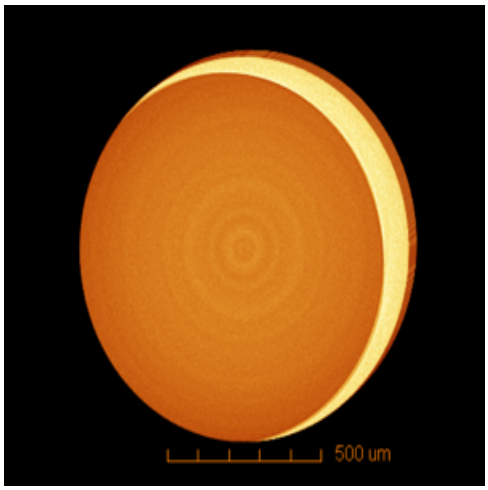

Figure 14. 3D view of sample 16 by microCT from the surface of the tube. The image represents the reconstruction error, ring artifact and yellow part shows the wall of the tube.

Moreover, filter paper coated with silver nanoclusters (sample 9-15) with different dipping time, imaged by microCT. Figure 15 represents the 2D and 3D view of microCT imaging of pile of filter paper. Remarkably, sample 7, the filter paper with longer dipping time of 2 hours show sufficient brightness which means it absorbed more X-ray energy during imaging. Broadly, the brightness can explain the accumulation of AgNC. Furthermore, by 3D visualization, it can be figured out that some parts of the sample 14 with even shorter dipping time (1 hour) looks bright. Although, sample 14 has less reliability owning to the fact that it dipped into AgNCs in ethanol (EtOH) and treated differently compared to other samples.

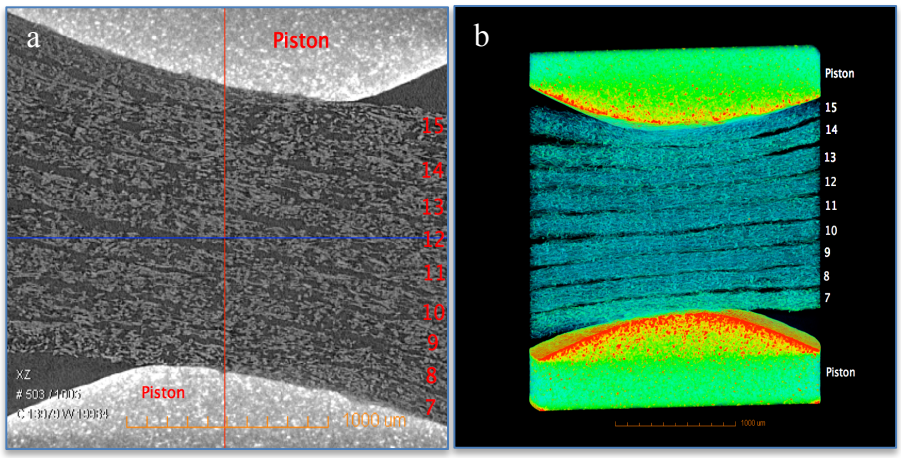

Figure 15. a. 2D view of Pile of Filter paper. b. 3D view of pile of filter paper coated with AgNCs. From 3D view, sample 7 looks brighter than any other filter paper since it has the longest dipping time of 2 hours.

4.2 Estimation of X-ray and light absorption of samples with the same amount of AgNC but different methods of preparation

In order to interpret the behavior of samples, bar graphs have been created from samples with the same amount of Ag but different approaches of preparation to evaluate the absorption of X-ray or fluorescent signal. To this aim, data (mean and median) obtained from microCT and OPT images to analyze the samples. Herein, bar graphs of all microCT images, and OPT images have been depicted to show how samples with the same ratio of AgNC behave after absorbing light or X-ray.

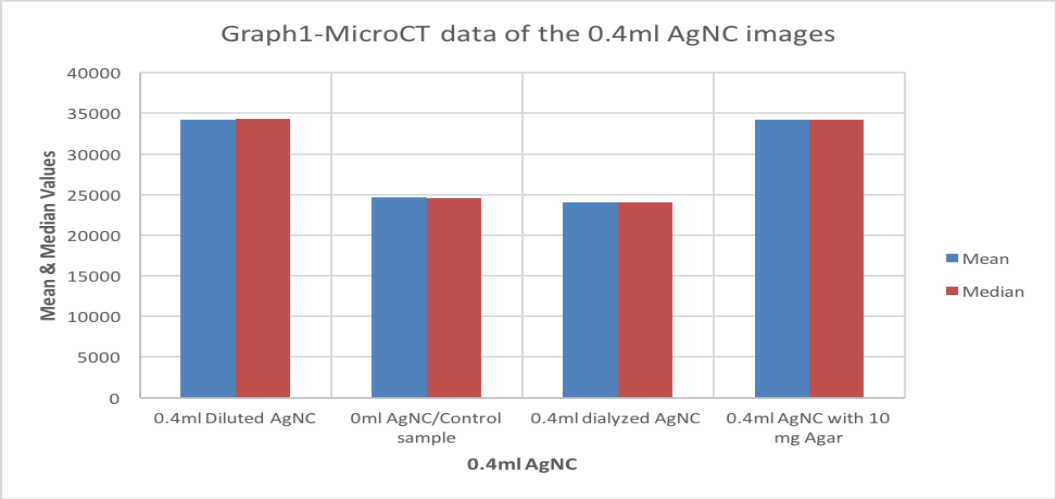

Figure 16. Estimation of X-ray absorption for all o.4 ml AgNC samples which prepared by different methods. 0.4 ml dialyzed AgNC sample shows lower X-ray absorption compared to other 0.4 ml AgNC samples

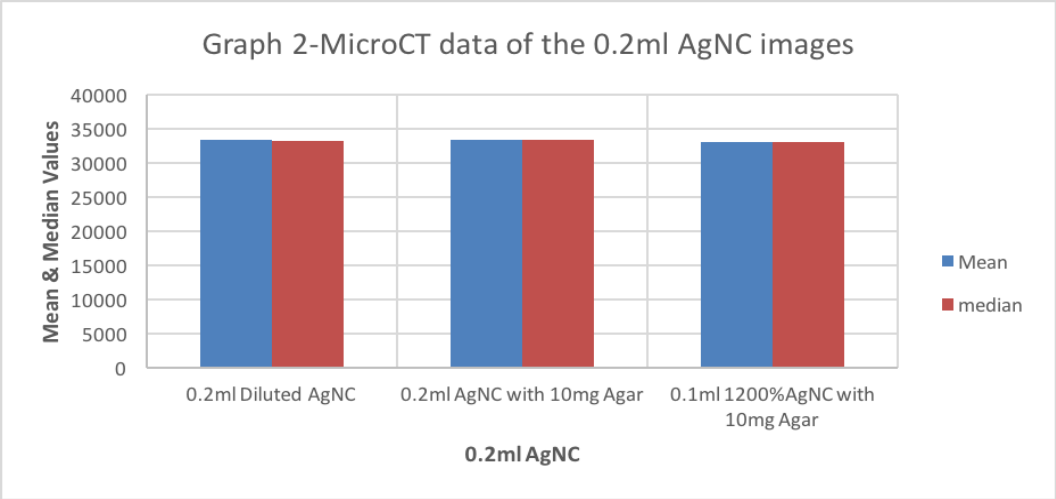

Figure 17. Estimation of X-ray absorption for all 0.2 ml AgNC samples which prepared by different methods show samples absorbed the same amount of X-ray

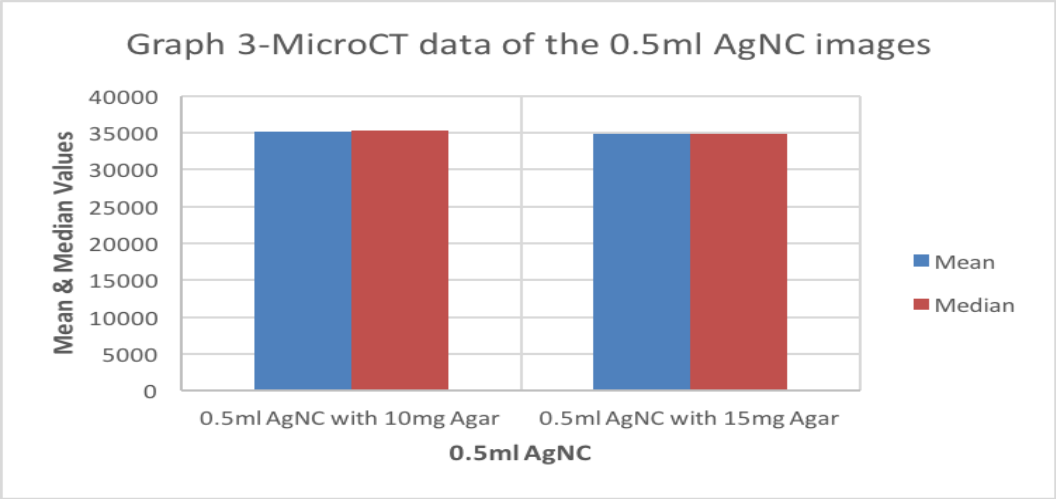

Figure 18. Results show the same amount of X-ray absorption for all 0.5 ml AgNC samples

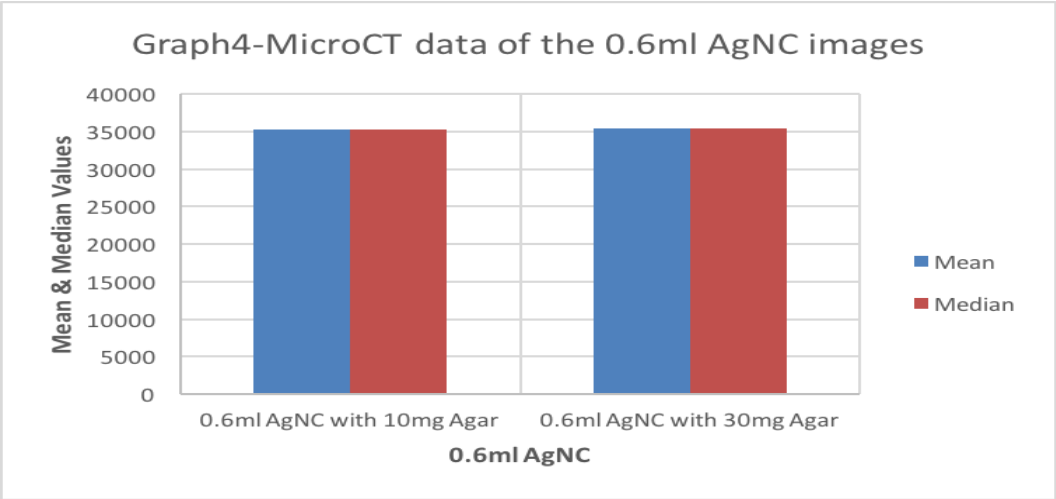

Figure 19. Results represent the same amount of X-ray absorption for all 0.6 ml AgNC samples

From the graphs above we got comparable results to see that all the samples with the same amount of AgNC, absorbed the similar level of X-ray energy except graph 1 which 0.4ml AgNC dialyzed sample showed lower values compare to other 0.4ml AgNC samples. It seems that the AgNC has been lost in 0.4ml AgNC dialyzed sample, since it shows even lower value than sample with 0ml AgNC.

Similarly, bar graphs, figures 20-23, created from OPT fluorescent imaging.
As figure 20 presents sample 0.4ml AgNC EtOH and 0.4ml AgNC dialyzed show the lower absorption of light. Figure 23 reveals that samples with higher amount of agar illustrates higher values. This means that samples with higher ratio of agar absorbed more light during fluorescent imaging.

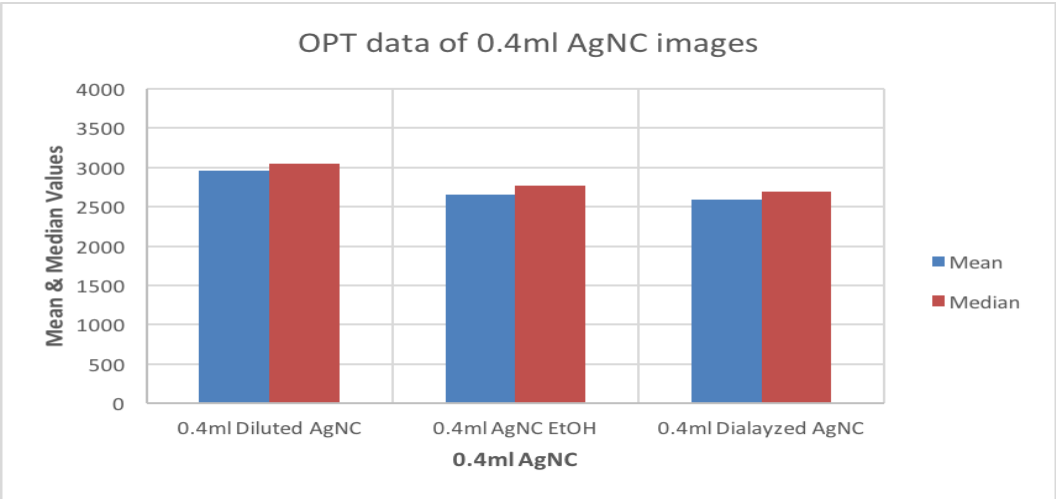

Figure 20. Results show that samples with the same amount of Ag (0.4 ml) but different methods of preparation (EtOH and dialyzed), absorbed lower light compared to diluted AgNC

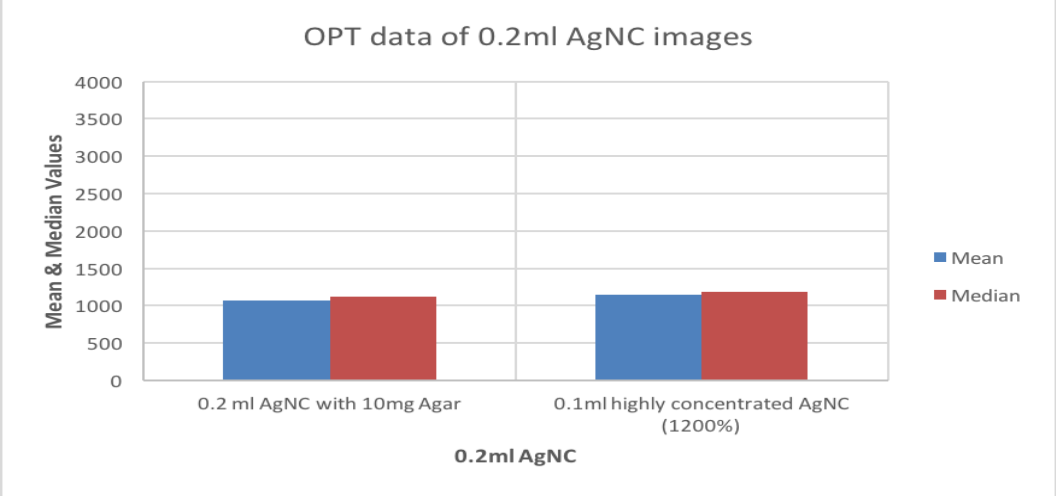

Figure 21. Results represent all the 0.2 ml AgNC samples absorbed the same level of light

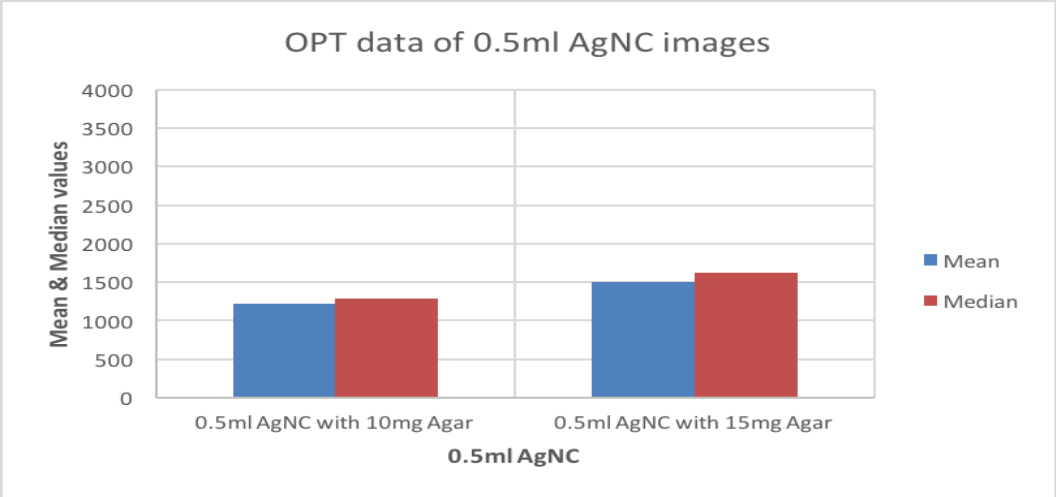

Figure 22. Results represent 0.5 ml AgNC samples which includes higher amount of agar absorbs more light

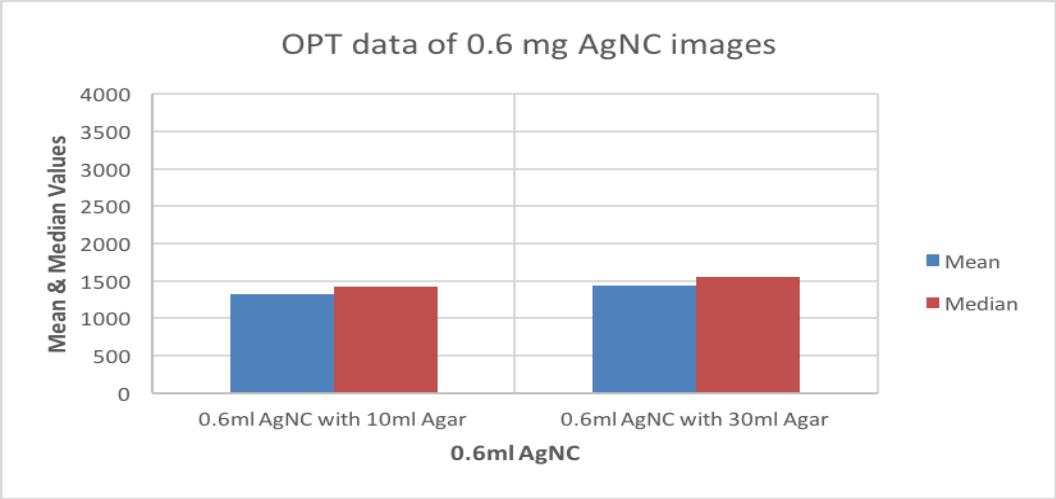

Figure 23. Results show 0.6 ml AgNC samples with higher amount of agar absorbs more light

Bar graphs of samples which imaged by OPT first then microCT have been attached to appendix 3. In these graphs, samples with 0.4ml AgNC EtOH and 0.4ml dialyzed AgNC show also lower absorption of X-ray.

4.3 Analyzing the relation between X-ray attenuation and light with the amount of Silver Nanoclusters

The graphs below demonstrate the correlation between the data obtained from microCT images (mean & median) and the ratio of AgNC in samples. As can be seen from the figure 24 most of the samples were distributed along the regression line except sample 0ml AgNC and 0.4ml dialyzed AgNC which act as outliers with the least values. It seems possible that these results are due to sample 0ml AgNC does not contain any AgNC and as it expected sample 6 (0.4ml Dialyzed AgNC) treated differently compared to other samples. Therefore, lower values show lower absorption of X-ray in these samples which means that these results are in consistent with the data obtained from bar graphs, figure 16. In both graphs sample 4 (0ml AgNC) and 6 (0.4ml dialyzed AgNC) act as outliers.

In this analysis sample 5 (0.4ml EtOH AgNC) is excluded since both tubes were imaged by OPT beforehand and third tube of sample 5 was destroyed already (no parafilm at one end). Mean & Median, estimated the amount of X-ray absorption for each sample. Thus, figure 24 displays the correlation of two independent values, microCT data and silver ratio vividly.

Mean and median values for each sample can be found precisely in appendix 4 and 5.

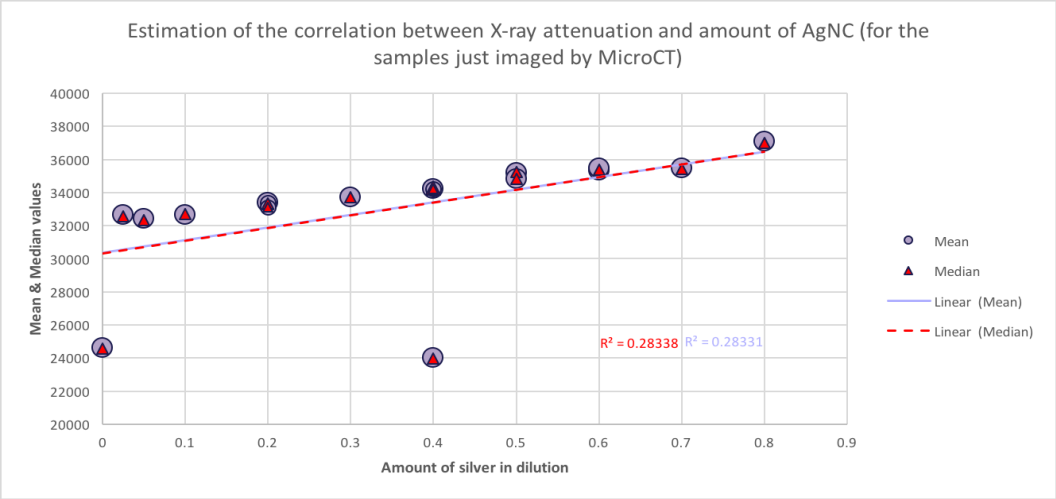

Figure 24. The results show the correlation between X-ray absorption and the silver concentration

In order to show how data, behave without the outliers, samples 4 and 6 were removed from the graph in figure 25. In this case linearity increased up to 96%.

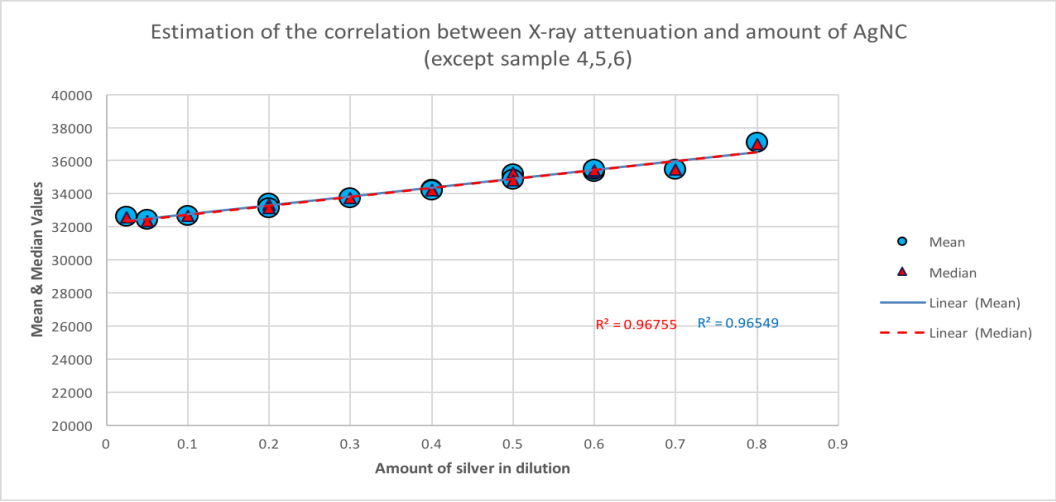

Figure 25. The results show the linear behavior between the data obtained from MicroCT images and AgNC ratio in samples by excluding the clear outliers

This picture confirms the ascending behavior of X-ray attenuation and the amount of AgNCs in samples. After that, data obtained from microCT imaging of samples which were imaged by OPT first. Figure 26 provides the behavior of samples which imaged by OPT first then microCT.

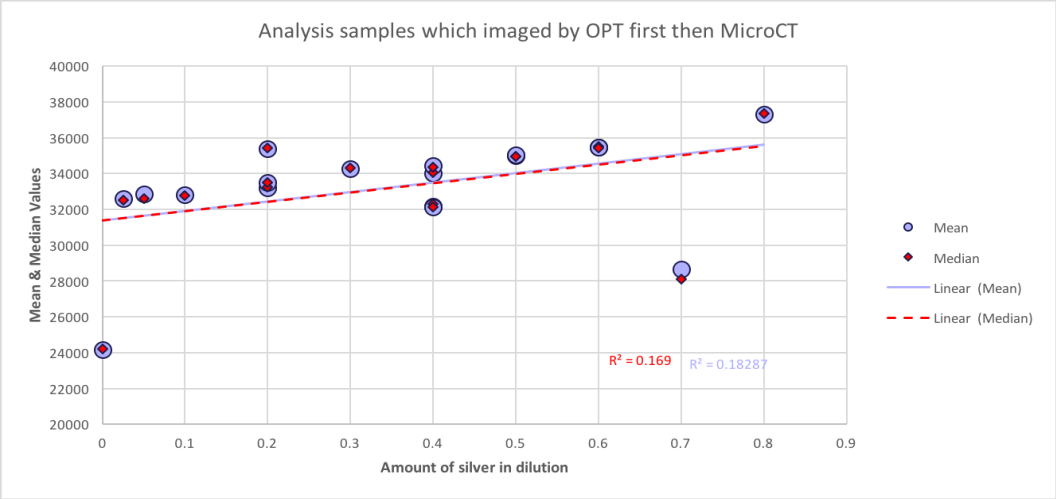

Figure 26. The graph displays the correlation between OPT-MicroCT data and amount of silver ratio in dilution

As shown in figure 26, sample 4 and 25 are quite apart from the distribution of data and regression line with the least values. Sample 4 contains 0ml AgNC_0.3ml agar and 0.4ml water. On the contrary, sample 25 has 0.7 ml AgNC with no Agar and water. Owning to the fact that possibly sample 25 degraded and precipitated by absorbing light during fluorescent imaging since there is no water or agar to support the AgNC and this leads sample 25 absorbs lower amount of X-ray during microCT imaging.

For the greater depth and breadth, a combined graph of microCT and OPT-MicroCT data has been created to compare how samples which imaged by microCT or first imaged by OPT then microCT behave. Figure 27 displays the combined graph without the outliers.

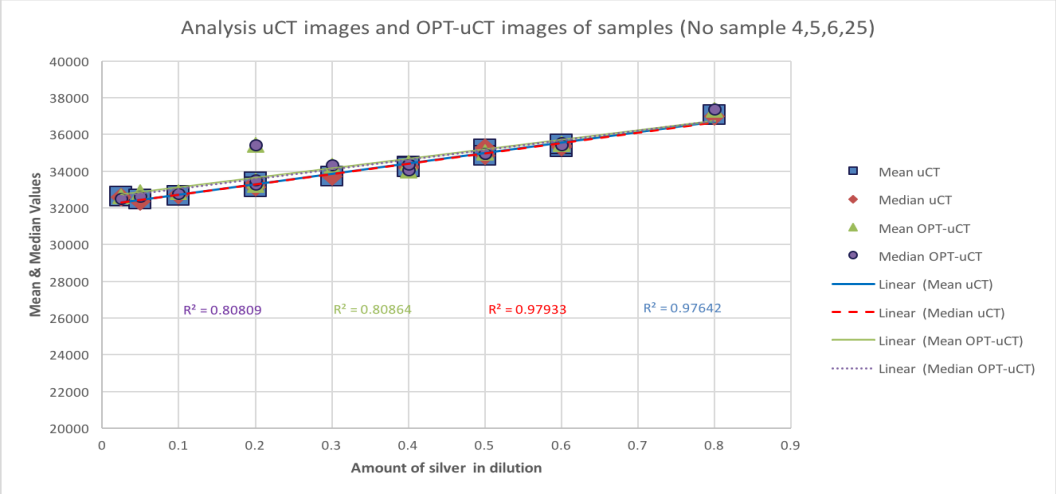

Figure 27. Combined graph of microCT images and samples which imaged by OPT first then microCT

The depicted graphs almost behave linearly in either case. Consequently, the graphs unveiled the fact that it does not matter whether samples first image by OPT or not, in either case, they behave linearly.

Furthermore, graphs have been illustrated from data of fluorescent images to present what is the relation between the light absorption and amount of silver nanoclusters. Since most of the samples turn to bleaching and get darker during fluorescent imaging and bleaching has an effect on the image quality.
Another key point about the graph is that, since it is required to implement fluorescent imaging in dark environment, samples 1-6 and 16-27 have been imaged in two different labs with different levels of light, that's why the graph from these samples have been drawn individually. The data from OPT imaging also demonstrate that there is a linear correlation with fluorescent imaging (light absorption) and amount of AgNCs in samples and it is presented in figure 28 and 29.

It worth mentioning that fluorescent materials activated in each fluorescent imaging by excitation the light, and it caused either darkening or photobleaching for most of the AgNCs-Agar samples. This phenomenon may alter the structure of AgNCs chemically, hence, OPT graphs show the data before darkening from non-changed structures inside the tube. All the mean and median values for each graph can be found in appendix.

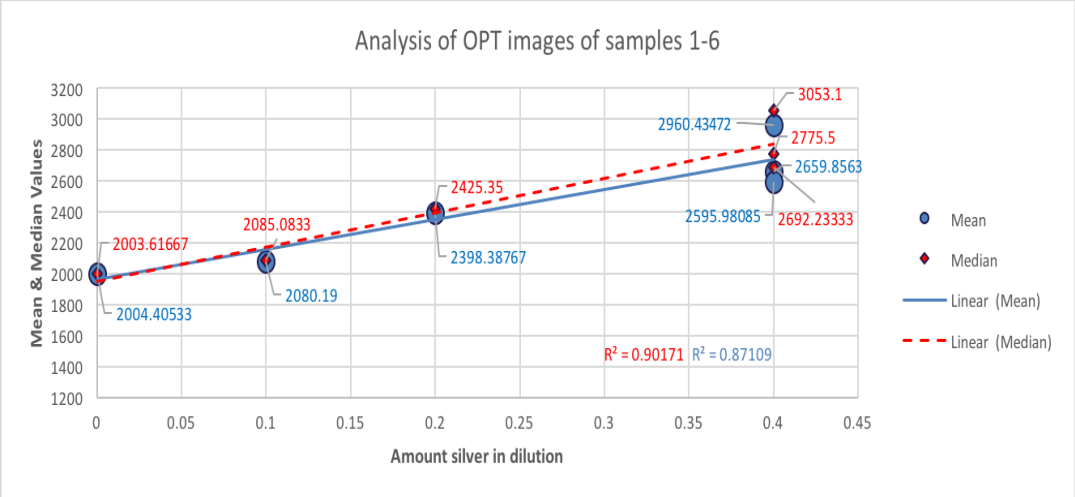

Figure 28. Results from samples 1-6 which imaged by fluorescent OPT show the amount of light absorption proportion to amount of Ag

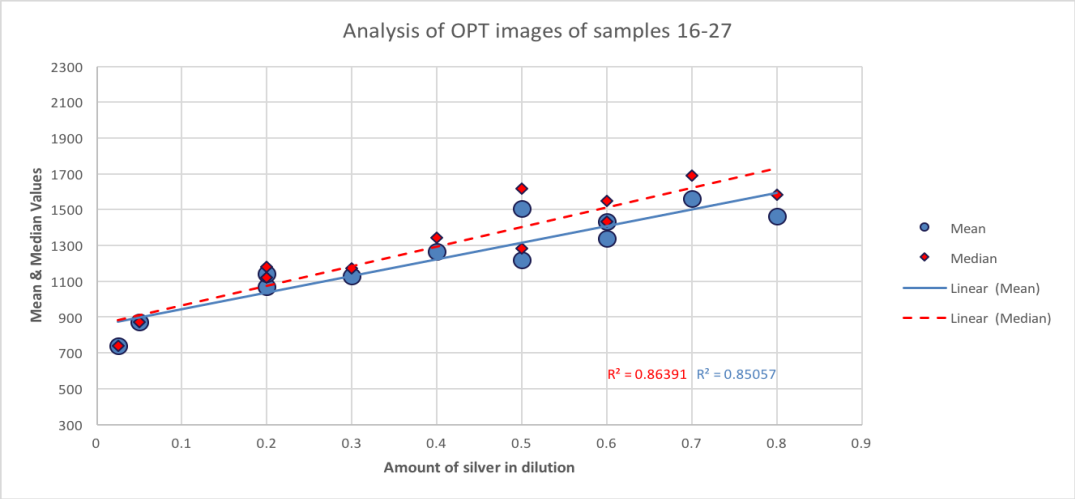

Figure 29. Results from samples 16-27 which imaged by fluorescent OPT shows the amount of light absorption proportion to amount of Ag

4.4 OPT images of AgNCs-Agar

In order to analyze the OPT images, data obtained from the fluorescent images with the same exposure time and this makes the analysis more comparable. Fluorescent silver nanocluster samples turned to darkening after absorbing light which this provides functional information for each sample.

Most of the samples in this study turned darker during imaging. This can be explained either as the chemical changes or photo-bleaching. Some samples showed strong darkening while some get darker smoothly during fluorescent imaging. On the other hand, samples formed intensive structure like cloud and some samples revealed granular structures after absorbing light. There is no more exact explanation of whether these structures formed due to just darkening and light absorption or the reason is due to signal decay and photo-bleaching. The structures are more apparent during bright field imaging which took after fluorescence imaging. There was an exceptional case for sample 25. This sample did not bleach during the fluorescent imaging although it contains 0.7 ml AgNCs without any water or agar. It seems that the same chemical reaction did not happen for the sample 25 as it happened for the rest of the samples.

Figure 30 displays the first, 200th and 400th frame of fluorescent imaging for samples 17, 25 and 27 respectively.

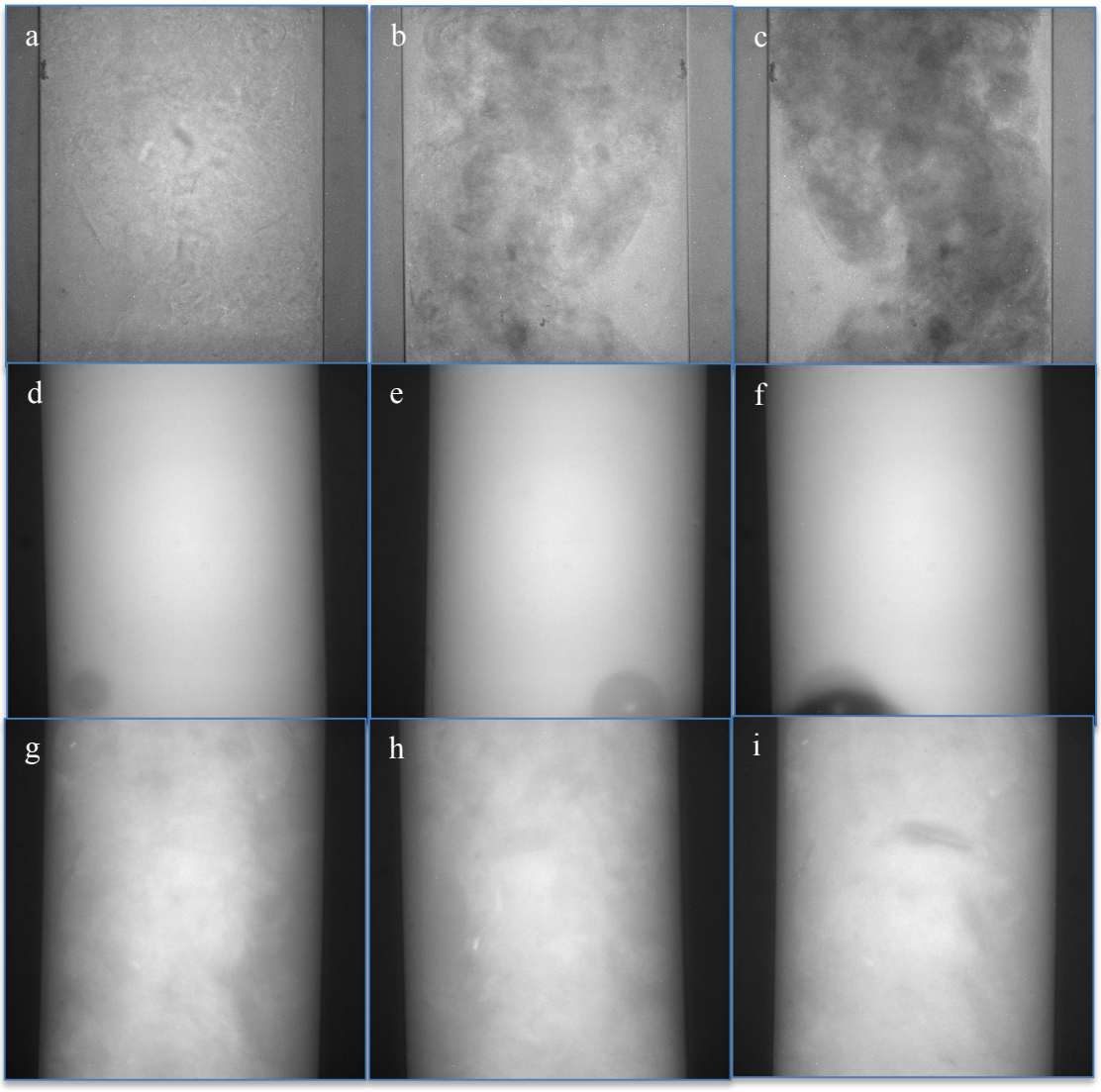

Figure 30. Fluorescent imaging of samples 17, 25, 27. a, b, c show the fluorescent imaging of sample 17 for the first frame, middle (200^{th}) frame and last (400^{th}) frame respectively. d, e, f display the first, middle and last frame for sample 25. g,h,i present the first ,middle and last frame of sample 27.

As can be presented from figure 30, fluorescent imaging of sample 17 comes along with forming cloud-shaped structure or so-called bulk at the end. Sample 25 did not formed darkening during the fluorescent imaging. It is difficult to explain this result but it is assumed that no agar and water in preparation of this sample plays an important role and the same chemical reaction did not happen for this sample compared to other sample during fluorescent imaging. Sample 27 showed granule-shaped structures after getting dark.

Bright field images of the named samples attached to appendix 7 to visualize the structures formed after fluorescent imaging vividly.

4.5 Analyzing the darkening behavior of Silver Nanoclusters in OPT

For more observations of the darkening or signal decay of samples during fluorescent imaging graphs have been created from the whole OPT projections (400 frames). Some of the samples such as 0.4ml AgNC_0mlH_2O_ 0.3ml Agar showed strong and faster darkening which may lead to photo-bleaching and some samples revealed smooth photo-bleaching like 0.025ml AgNC_0.375mlH_2O _0.3ml Agar.

The graphs depicted from the fluorescent imaging are presented in figures 31 and 32. A dashed vertical line in both graphs displays the first 60 projections roughly, which figure 31 and 32 have been created from the data before the tubes turn to darkening and form different structures.

In general, most of the samples turn to darkening after absorbing light except samples 2 (0.2 ml AgNC_0.2ml H_2O_0.3ml Agar), sample 23 (0.5ml AgNC_0 mlH_2O _ 0.2ml Agar), sample 25 (0.7ml AgNC_0ml H_2O _0 ml Agar) which did not turn bleaching during fluorescent imaging.

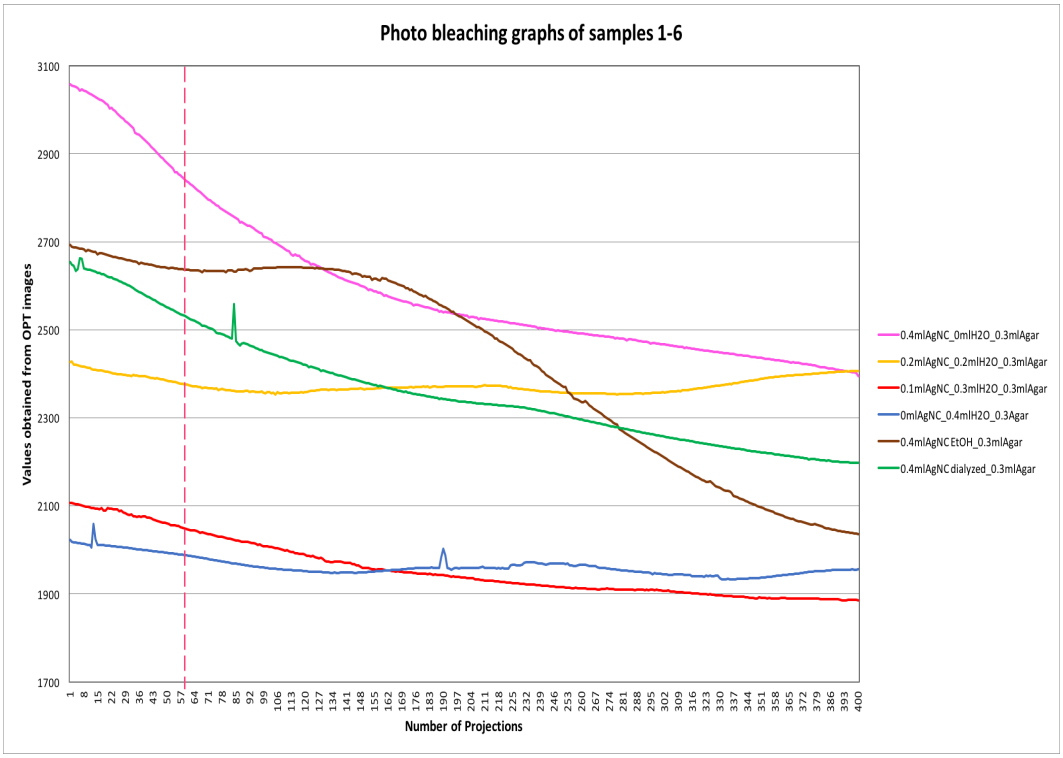

Figure 31. The graphs display the whole darkening behavior in fluorescent OPT for samples 1-6

Graphs for samples with 0ml AgNC and 0.4ml AgNC dialyzed AgNC contain some noises (spikes) which referred to the lab where it was not completely dark during the fluorescent imaging due to the light interference. Contrary to these samples, samples 16-27 display smooth and very small darkening which can be followed from figure 32.

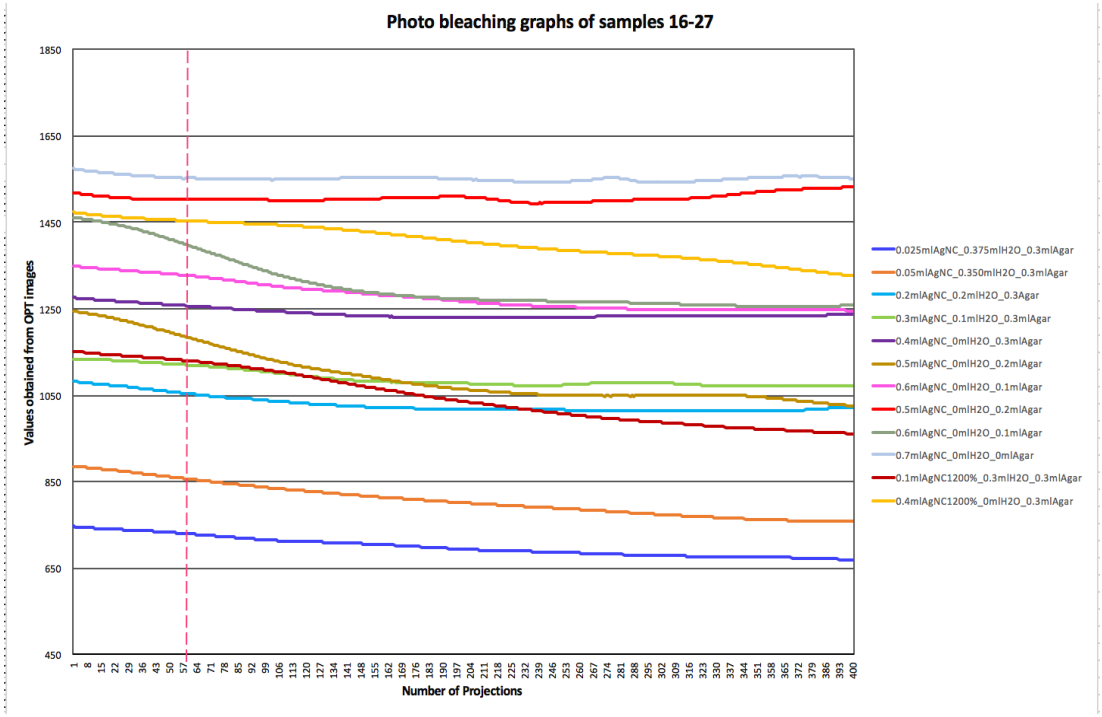

Figure 32. The graphs display the whole darkening behavior in fluorescent OPT for samples 16-27

5.CONCLUSIONS

In sum, one evident result emerged from the data is that X-ray attenuation in microCT imaging and fluorescent signal in OPT imaging acts as a linear function with the amount of silver nanoclusters in samples. This fact confirmed the dual functionality of fluorescent silver nanoclusters as a contrast agent in multimodal imaging of X-ray and optical imaging.

Additionally, data from obtained images unveiled that it does not significantly matter whether samples imaged by OPT first or just imaged by microCT, in either case, there is a linear correlation between X-ray attenuation and the ratio of silver nanoclusters in samples. From the microCT analysis samples 4, 5 and 6 and 25 acted as outliers in depicted graphs. Sample 4 does not include any AgNC, sample 5 and 6 contain 0.4 ml EtOH AgNC and 0.4 ml dialyzed AgNC, respectively which were prepared differently compared to other samples. Thus, they absorbed less X-ray energy. This might be due to the way sample 4 & 6 have been processed, maybe during purification steps more silvers have been precipitated in these samples, that's why it causes less X-ray absorption during imaging. Lastly, sample 25 with no agar and water showed also less absorption of X-ray in figure 26.

From the observations of OPT imaging, most of the samples exhibited darkening and formed cloudiness or granular shaped structures in both emission and transmission OPT images. It is not clear why exactly this darkening happened. One possible explanation could be that AgNC was destructed during OPT imaging and it broke into Ag ions or molecules which exhibited a darkening in images. It worth noting that sample 25 (0.7ml AgNC) did not turn to darkening during fluorescent OPT imaging. This sample displayed completely distinct behavior which did not show any cloudiness structures during the fluorescent imaging with also quite vivid images of bright-field imaging. Maybe, different behavior of sample 25 can be explained in a way that it was not diluted with any water or agar. In general, data obtained from OPT imaging are in line with the X-ray microtomography and corroborate the linearity in both imaging modalities.

Since more concentrated AgNCs samples including samples without water or agar dilution are required to evaluate the light and X-ray absorption accurately, there is not exact explanation of different behaviors of outliers from the microCT graph whilst this should be taken into account that samples used in this study contained different amounts of agar and water and this might affect the Ag nanoclusters' behavior and causing

different formed structures in the tube after light absorption. There is still no clue that whether signal decayed or just chemical changes lead to sample darkening.

Notwithstanding the relatively limited samples, this work offers valuable insights into metal nanoclusters, particularly fluorescent AgNCs as multimodality imaging label. The overview of work proved that there is a correlation between X-ray attenuation and fluorescent signal with the ratio of silver. However, fluorescent silver nanoclusters suffer from instability and they are prone to photo-bleaching and maybe destruction of the cluster structure.

Taken together, in this study, we could detect both fluorescent and X-ray signals from images and approved the novel silver nanoclusters as substitution for contrast agent in bioimaging since they show contrast for optical imaging and X-ray microtomography.

It is worth mentioning that fluorescent metal nanoclusters are novel concepts and classifications of luminescent nanomaterials. Investigations in this field are still in progress owning to their different functionalities such as optical properties for applications like contrast agent in imaging and bioanalysis (Shang et al.2011) and fluorescent probes in molecular sensing (Diez et al.2009).

Despite the widespread literatures on fluorescent nanoclusters, this subject is still in an early stage and much practical works have been remained to employ them on feasible applications. However, we were able to show the fluorescent silver nanoclusters as contrast agent in both fluorescent optical imaging and X-ray imaging. This approach introduces the novel use of fluorescent silver nanoclusters as label for biological imaging of low contrast samples.

REFRENCES

Abu Anas Emran M, Kim Jae G, Lee Soo Y, Hasan MD K, **Comparison of ring artifact removal methods using flat panel detector based CT images**, BioMedical Engineering OnLine, 2011, Vol.10, pp.1-25

Als-Nielsen Jens, **X-rays and matters- the basic interactions**, C.R Physiques, 2008, Vol 9, pp.479-486

Attix Frank Herbert, **Introduction to Radiological Physics and Radiation Dosimetry**, 1986, Wiley-VCH Wisconsin, USA, 599 p

Axelsson Maria, Svensson Stina, Borgefors Gunilla, **Reduction of Ring Artifacts in High Resolution X-ray Microtomography Images,** Pattern Recognition, 2006, DAGM, Vol 4174, pp.61-70

Barret Julia F, Keat Nicholas, **Artifacts in CT: Recognition and Avoidance**, RadioGraphics, 2004, Vol.24, No.6, pp.1679-1691

Betz Oliver, Wegst Ulrike, Weide Daniela, Heethoff Michael, Helfen Lukas, Lee Wah-Keat, Cloetens Peter, **Imaging applications of synchrotron X-ray phase-contrast microtomography in biological morphology and biomaterials science. I . General aspects of the technique and its advantages in the analysis of millimeter-sized arthropod structure**, Journal of Microscopy, 2007, Vol.227, pp.51-71

Beutel Jacob, Kundel Harold L., Van Metter Richard L., **Handbook of Medical Imaging**, Physics and Psychophysics, SPIE Press Washington, 2000, Vol.1, USA, 931 p

Birk Udo Jochen, Rieckher Matthias, Konstantin ides, Darrell Alex, Sarasa-Renedo Ana, Meyer Heiko, Tavernarakis Nektarios, Ripoll Jorge, **Correction for Speciment movement and rotation errors for in-vivo Optical Projection Tomography**, 2010, Vol.1, Issue.1, pp.87-96

Blanquer S B, Werner M, Hannula M, Sharifi S, Lajoinie GP, Eglin D, Hyttinen J, Poot AA, Grijpma DW. **Surface curvature in triply-periodic minimal surface**

architectures as a distinct design parameter in preparing advanced tissue engineering scaffolds. Biofabrication, D. W. 2017, Vol.9, No.2, 025001

Boas F Edward, Fleischmann Dominik, **CT artifacts: causes and reduction techniques**, Imaging Med, 2012, Vol. 4, Issue.2, pp.229-240

Bushberg Jerrold T, Seibert J.anthony, Leidholdt Edwin M.Jr, Boone John M, **The Essential Physics of Medical Imaging**, 2012, Third Edition, Wolters Kluwer Philadelphia, USA, 1005 p

Chen Lingling, McGinty James, Taylor Harriet B., Bugeon Laurence, Lamb Jonathan R., Dallman Margaret J., French Paul M.W., **Incorporation of an experimentally determined MTF for spatial frequency filtering and deconvolution during optical projection tomography reconstruction,** OPTICS EXPRESS, 2012, Vol.20, No.7, pp.7323-7337

Davis G.R., Elliott J.C., **Artefacts in X-ray microtomography of materials,** Materials Science and Technology, 2006, Vol.22, No.9, pp.1-9

Diez Isabel, Pusa Matti, Kulmala Sakari, Jiang Hua, Walther Andreas, Goldmann Anja S., Muller Axel H.E., Ikkala Olli, Ras Robin H.A., **Color Tunability and Electrochemiluminescence of Silver Nanoclusters**, Angewandte Chem Int Ed, 2009, Vol.48, Issue.12, pp.2122-2125

Diez Isabel, Ras Robin H.A., **Few-Atom Silver Clusters as Fluorescent Reporters**, Advanced Fluorescence Reporters in Chemistry and Biology II, Molecular Constructions, Polymers and Nanoparticles, Springer Ser Fluoresc, 2010, Vol.9, pp.307-332

Diez Isabel, Eronen Paula, Osterberg Monika, Linder Markus B., Ikkala Olli, Ras Robin H.A., **Functionalization of Nanofibrillated Cellulose with Silver Nanoclusters: Fluorescence and Antibacterial Activity**, Macromolecular Bioscience, 2011, Vol.11, Issue. 9, pp.1185-1191

Diez Isabel, Ras Robin H.A., **Fluorescent Silver Nanoclusters,** Nanoscale, 2011, Vol.3, pp.1963-1970

Dong Di, Zhu Shouping, Qin Cheghu, Kumar Varsha, Stein Jens V., Oehler Stephan, Savakis Charalambos, Tian Jie, Ripoll Jorge, **Automated Recovery of the Center of Rotation in Optical Projection Tomography in Presence**, IEEE JOURNAL OF BIOMEDICAL AND HEALTH INFORMATICS, 2013, Vol.17, No.1, pp.198-204

D'Acunto Mario, Benassi Antonio, Moroni Davide, Salvetti Ovidio, **3D image reconstruction using Radon transform**, SIViP, 2016, Vol.10, pp.1-8

Etrych Tomas, Lucas Henrike, Janouskova Olga, Chytil Petr, Mueller Thomas, Mäder Karsten, **Fluorescence optical imaging in anticancer drug delivery,** Journal of Controlled Release, 2016, Vol.226, pp.168-181

Figueiras Edite, Soto Ana M., Jesus Danilo, Lehti M., Koivisto J., Parraga J.E., Silva-Correia J., Oliveira J.M., Reis R.L., Kellomaki M., Hyttinen J., **Optical projection tomography as a tool for 3D imaging of hydrogels**, BIOMEDICAL OPTICS EXPRESS, 2014, Vol.5, No.10, pp.3443-3449

Gao Shengping, Chen Donghua, Li Qiwei, Ye Jing, Jiang Hui, Amatore Christian, Wang Xuemei, **Near-infrared fluorescence imaging of cancer cells and tumors through specific biosynthesis of silver nanoclusters**, SCIENTIFIC REPORTERS, 2014, Vol.4, No.4384, pp.1-6

Holdsworth David W. & Thornton Michael M., **Micro-CT in small animal and specimen imaging,** 2002, Trend in Biotechnology, Vol.20, No.8, pp. S 34-S 39

Hsieh Jiang, **Computed Tomography. Principles, Design, Artifacts and Recent Advances**, Second Edition, Wiley Inter-science & SPIE Press, 2009, Washington, USA, 551 p

Kak Avinash C., Slanely Malcolm, **Principles of Computerized Tomographic Imaging**, Chapter 5; Aliasing Artifact and Noise in CT Images, 1988, IEEE Press New York, USA, 329 p

Landis Eric N., Keane Denis T., **X-ray microtomography**, Materials Characterization, 2010, Vol.61, Issue.12, pp.1305-1316

Li Hao, Zhang Hui, Tang Zhiwei, Hu Guangshu, **Micro-computed tomography for small animal Imaging: Technological details,** Progress in Natural Science, 2008, Vol.18, Issue.5, pp.513-521

Lichtman Jeff W, Conchello Jose-Angel, **Fluorescence microscopy**, Nature Methods, 2005, Vol.2, No.12, pp.910-919

Liu Hui, Wang Han, Guo Rui, Cao Xueyan, Zhao Jinglong, Luo Yu, Shen Mingwu, Zhang Guixiang, Shi Xiangyang, **Size-controlled synthesis of dendrimer-stabilized silver nanoparticles for X-ray computed tomography imaging applications**, Polymer Chemistry, 2010, Vol.1, Issue. 10, pp.1677-1683

Lukianova-Hleb Ekaterina Y.,Kim Yoo-Shin, Belatsakouski Ihor, Gillenwater Ann M.,O'Neill Brian E., Lapotko Dmitri O., **Intraoperative diagnostics and elimination of residual microtumours with plasmonic nanobubbles**, Nature Nanotechnology, 2016,Vol 11, pp.525-532

Meagher J.M., Mote C.D, JR., Skinner H. B., **CT Image Correction for Beam Hardening Using Simulated Projection Data**, IEEE TRANSACTIONS ON NUCLEAR SCIENCE, 1990, Vol. 37, No.4, pp.1520-1524

Metscher Brian D**, MicroCT for comparative morphology: simple staining methods allow high-contrast 3D imaging of diverse non-mineralized animal tissues,** BMC physiology, 2009, Vol. 9(1): 11, pp.1-14

Metscher Brian D, Muller Gerd B., **MicroCT for Molecular Imaging: Quantitative Visualization of complete three-Dimensional Distributions of Gene Products in Embryonic Limbs**, Developmental Dynamics, 2011, Vol. 240, Issue.10, pp.2301-2308

Michail C.M, Karpetas G.E., Fountos G.P., Valais I.G., Nikolopoulos D., Kandarakis I.S., Panayiotakis G.S., **Assessment of the Contrast to Noise Ratio in PET Scanners with Monte Carlo Methods**, Journal of Physics, 2015, Vol.637, pp.1-4

MicroXCT-200 and MicroXCT-400, 2010, User's Guide, Xradia, CA, USA, 283 p, Document Part Number: G000408

Mizutani Ryuta, Suzuki Yoshio, **X-ray microtomography in biology**, Micron, 2012, Vol.43, pp.104-115

Morrison John C, **Modern Physics for scientists and Engineers**, Elsevier, 2010, USA, 445 p

Narra N, Blanquer SBG, Haimi SP, Grijpma DW, Hyttinen J. **μCT based assessment of mechanical deformation of designed PTMC scaffolds.** Clinical Hemorheology and Microcirculation, 2015, Vol.60, No.1, pp. 99-108

Pawley James B., **Handbook of Biological Confocal Microscopy**, Third Edition, Chapter 39: Photobleaching, Springer Science + Business Media, 2006, LLC, New York, 933 p

Ravalli Andrea, Voccia Diego, Palchetti Ilaria, Marrazza Giovanna, **Electrochemical, Electrochemiluminescence, and Photoelectrochemical AptamerBased Nanostructured Sensors for Biomarker Analysis**, biosensors, 2016, Vol.6, Issue 39, pp.1-20

Ristic Goran, **The Digital Flat-Panel X-ray Detectors**, Third conference on medical physics and biomedical engineering, 2013, Vol.45, Issu.10, pp.65-71

Rossman Kurt, **Point Spread Function, Line Spread-Function and Modulation Transfer Function**, 1969, Vol.93, pp.257-272

Schambach Sebastian J, Bag Simona, Schilling Lothar, Groden Christoph, Brockmann Marc A., **Application of micro-CT in small animal imaging**, Methods, 2010, Vol.50, Issue.1, pp.2-13

Scherl Holger, Kowarschik Markus, Hofmann Hannes G., Keck Benjamin, hornegger Joachim, **Evaluation of State-of-the-Art Hardware Architectures for Fast Cone-Beam CT Reconstruction**, Parallel Computing, 2012, Vol.38, Issue.3, pp.111-124

Schulze R, Heil U, Groβ D, Bruellmann DD, Dranischnikow E, Schwanecke U, Schoemer E, **Artifacts in CBCT: a review**, Dentomaxillofacial Radiology, 2011, Vol. 40, pp.265-273

Shang Li, Dong Shaojung, Nienhaus G. Ulrich, **Ultra-small fluorescent metal biological applications**, Nanotoday, 2011, Vol.6, Issue. 4, pp.401-418

Sharpe James, Ahlgren Ulf, Perry Paul, Hill Bill, Ross Alyson, Hecksher-sorensen Jacob, Baldock Richard, Davidson Duncan, **Optical Projection Tomography as a Tool for 3D Microscopy and Gene Expression Studies**, SCIENCE, 2002, Vol.296, pp.541-545

Sharpe James, **Optical projection tomography as a new tool for studying embryo anatomy**, Anatomical Society of Great Britain and Ireland, 2003, Vol.202, pp.175-181

Smith Steven W., **The Scientist and Engineer's Guide to Digital Signal Processing**, Second Edition, chapter 25. Special Imaging Technique, 1999, California Technical Publishing, USA, 643 p

Smyth M.S, Martin J.H.J, **X-ray Christallography**, Mol Pathol 2000, Vol.53, No.1, pp.8-14

Soret Marine, Bacharach Stephen L., Buvat Irene, **Partial-Volume Effect in PET Tumor Imaging**, The Journal of Nuclear Medicine, 2007, Vol. 48, No. 6, pp.932-945

Soto Ana M, Koivisto Janne T, Parraga Jenny E, Silva-Correia Joana, Oliveira Joaquim M, Reis Rui L, Kellomäki Minna, Hyttinen Jari, Figueiras Edite, **Optical Projection Tomography Technique for Image Texture and Mass Transport Studies in Hydrogels Based Gellan Gum,** Langmuir, 2016, Vol.32, No.20, pp.5173-5182

Stock S.R, **X-ray Microtomography of Materials**, International Materials Reviews, 1999, Vol.44, No.4, pp.141-164

Stock Stuart R., **MicroComputed Tomography, Methodology and Applications**, CRC Press, 2009, Boca Raton Florida, USA, 319 p

Van Grieken Rene E., Markowicz Andrzej A., **Handbook of X-ray Spectrometry, Methods and Techniques**, Marcel Dekker, 2002, New York Basel, 693 p

Walls J. R., Sled J. G., Sharpe J. and Henkelman R. M., **Correction of artefacts in optical projection tomography**, Phys. Med. Biol., 2005, Vol. 50, No.19, pp. 4645-4665

Walls J.R, Sled John G, Sharpe James, Henkelman R Mark, **Resolution improvement in emission optical projection tomography**, phys.Med.Biol, 2007, Vol.52, pp.2775-2790

Webb Andrew, **Introduction to Biomedical Imaging**, Wiley-IEEE press, 2003, 264 p

Welvaert Marijke, Rosseel Yves, **On the Definition of Signal-To-Noise Ratio and Contrast-To-Noise Ratio for fMRI Data**, PLoS One, Vol.8, Issue.11, 2013, pp.1-10

Willekens Inneke, Van de Casteele Elke, Buls Nico, Temmermans Fredrik, Jansen Bart, Deklerck Rudi, de Mey Johan, **High-resolution 3D micro-CT imaging of breast microcalcifications: a preliminary analysis,** BMC Cancer, 2014, Vol 14:9, pp.1-10

Wu Xu, He Xiaxiao, Wang Kemin, Xie Can, Zhou Bing, Qing Zhihe, **Ultrasmall near-infrared gold nanoclusters for tumor fluorescence imaging in vivo**, Nanoscale, 2010, Vol.2, pp.2244-2249

Yang Yujie, Di Dong, Shi Liangliang, Wang Jun, Hui Hui, Yang Xin, Tian Jie, **A preliminary study on a dual-modality OPT/micro-CT system,** Proc.SPIE**,** Vol.9328, pp.1-7

Xu Hangxun, Suslick Kenneth S., **Water-Soluble Fluorescent Silver Nanoclusters,** Advanced Materials, 2010, Vol.22, pp.1078-1082

Zhang Yongbin, Zhang Lifei, Zhu Ronald, Lee Andrew K, Chambers Mark, Dong Lei, **Reducing Metal Artifacts in Cone-beam CT Images by Preprocessing Projection Data**, Int. J. Radiation Oncology Biol. Phys., 2007, Vol.67, No.3, pp.924-932

Zheng Jie, Dickson Robert M., **Individual Water-Soluble Dendrimer-Encapsulated Silver Nanodot Fluorscence,** J. AM. CHEM. SOC., 2002, Vol. 124, No.47 , pp.13982-13983

Zhu Shouping, Dong Di, Birk Udo Jochen, Rieckher Matthias, Tavernarakis Nektarios, Qu Xiaochao, Liang jimin, Tian Jie, Ripoll Jorge, **Automated Motion Correction for in Vivo Optical Projection Tomography**, IEEE TRANSACTIONS ON MEDICAL IMAGING, 2012, Vol.31, No.7, pp.1358-137

Zou J, Hannula M, Misra S, Feng H, Labrador RH, Aula AS et al. **Micro CT visualization of silver nanoparticles in the middle and inner ear of rat and transportation pathway after transtympanic injection**, Journal of Nanobiotechnology, 2015, Vol.13, pp.1-9

Zou J, Pyykkö I, Hyttinen J. **Inner ear barriers to nanomedicine-augmented drug delivery and imaging**. Journal of Otology, 2016, Vol.11, pp. 165-177

150kV Microfocus X-ray Source L8121-01 datasheet, Hamamatsu Corporation, 2001, Japan, 4 p, TLSO1042E02. Available: http://pdf1.alldatasheet.com/datasheet-pdf/view/62642/HAMAMATSU/L8121-01.html

iKon-L _936 Series datasheet , ANDOR an Oxford Instruments company, 6 p, LiKonLSS 0716 R1, Available: http://www.andor.com/pdfs/specifications/Andor_iKon-L_936_Specifications.pdf

Appendix 1: Tables of MicroCT Imaging

Samples	Source distance	Detector distance	Pixel size	kV/W	Number of images	Exposure time	Total scanning time	Filter	Angle range	Camera binning	Objective
AgNCs-Agar in tubes	40mm	8mm	1.13 um	40/10	1600	14 s	22h	none	360	2	20X

Table A1.1 parameters used for microCT imaging of AgNCs-Agar samples

Samples	Source distance	Detector distance	Pixel size	kV/W	Number of images	Exposure time	Total scanning time	Filter	Angle range	Camera binning	Objective
Filter paper	100mm	10mm	2.5 um	50/10	1600	20 s	19.5h	none	360	2	10X

Table A1.2 Parameters used for MicroCT imaging of filter paper coated with AgNCs

Appendix 2: 2D visualization of sample 26 by MicroCT from three different fields of view

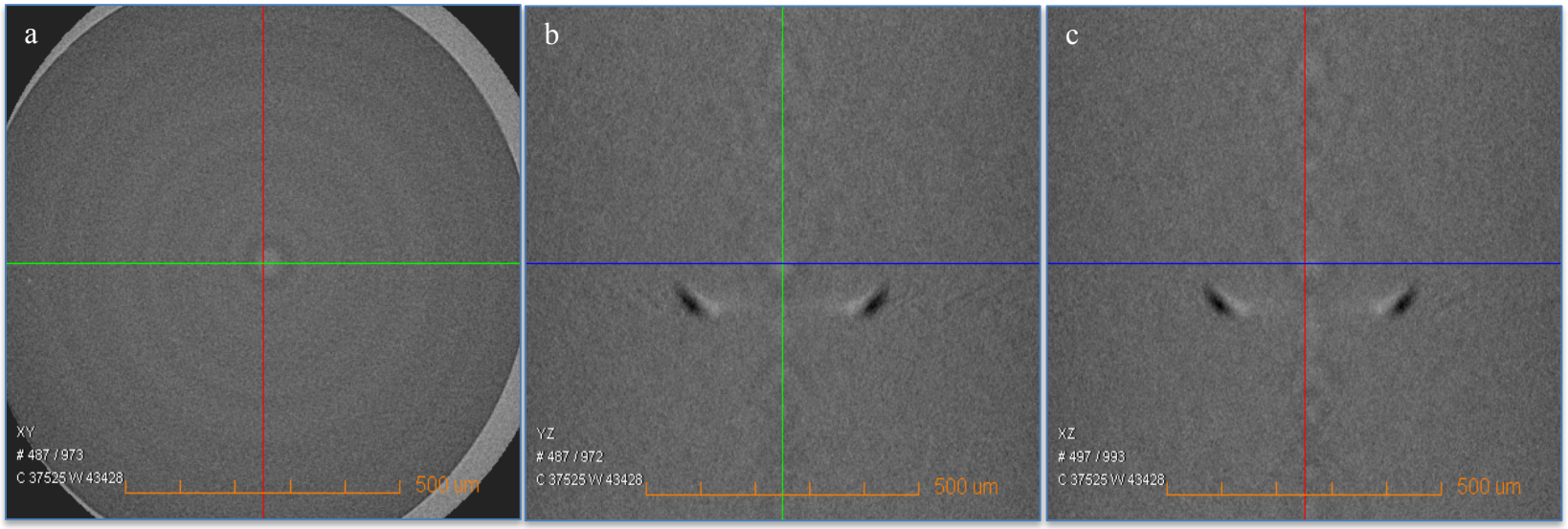

Figure A2.1 2D visualization of sample 26 by MicroCT imaging from different fields of view. a) XY view. b) YZ view. c) XZ view. There are two small black spots on b & c which they refer to dusts on the lens during imaging. Ring artifact is clear on a and cross-section of ring artifact on b & c along the green line. Furthermore, there is noise on the images which deteriorated the grayscale.

Appendix 3: Bar graphs from samples which imaged by OPT first then microCT

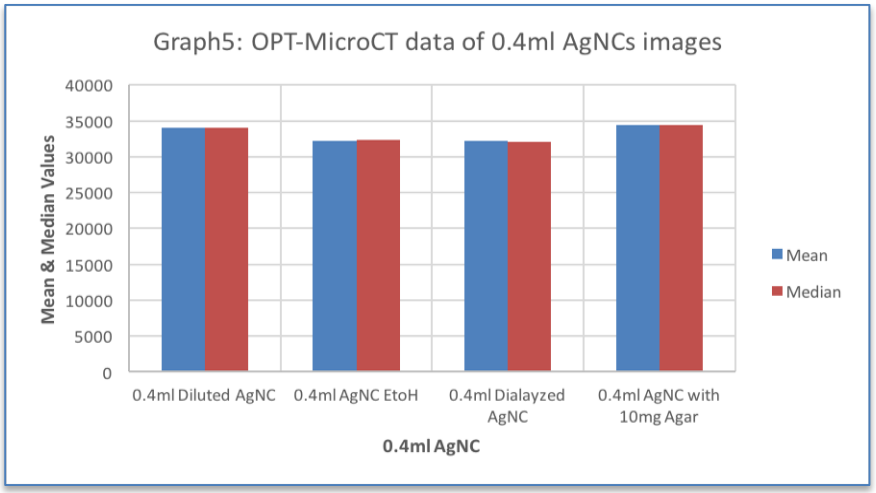

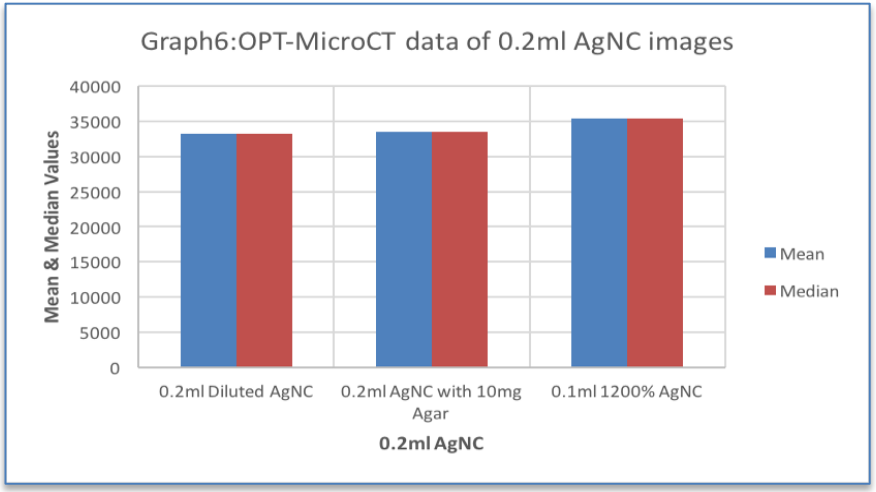

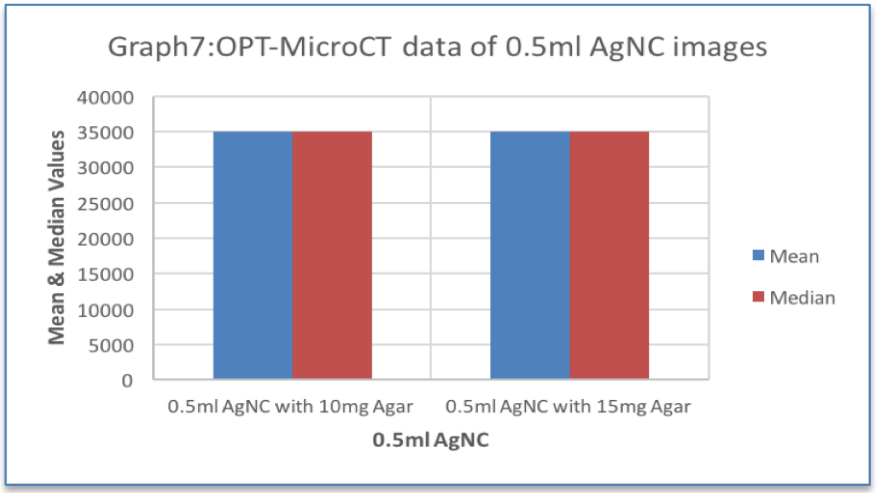

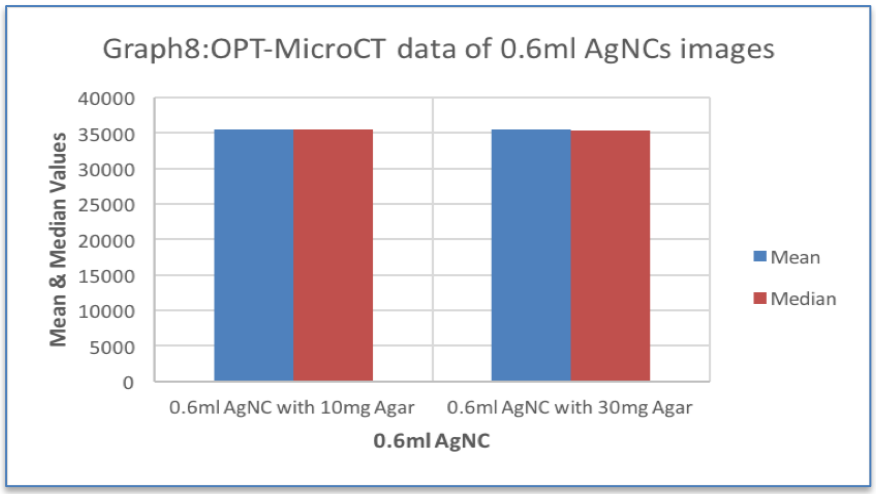

Appendix 4: Table of data (Average and Median) obtained from microCT images

samples	Amount of silver	Average	Median
1	0.4	34236.4771	34266
2	0.2	33384.663	33324
3	0.1	32647.3114	32683
4	0	24604.7686	24586
6	0.4	24004.2914	23983
16	0.025	32633.6657	32571.5
17	0.05	32446.35	32348.5
18	0.2	33387.52	33349.5
19	0.3	33718.21	33720
20	0.4	34198.0257	34192
21	0.5	35191.55	35262
22	0.6	35320.87	35299
23	0.5	34845.13	34824
24	0.6	35453.19	35401.5
25	0.7	35481.16	35446
26	0.2	33114.5	33114
27	0.8	37071.45	36979

Table A4.1 data obtained from microCT images

Appendix 5: Table of data (Average and Median) obtained from microCT images of OPT imaged tube

Samples	Amount of silver	Average	Median
1	0.4	34025.99	34046.5
2	0.2	33224.863	33261.5
3	0.1	32839.63	32787.5
4	0	24154.81	24201.5
5(EtoH)	0.4	32192.64	32294.5
6(dia)	0.4	32140.34	32138
16	0.025	32600.68	32514.5
17	0.05	32847.18	32605
18	0.2	33486.28	33503.5
19	0.3	34296.03	34332
20	0.4	34429.16	34368
21	0.5	35013.48	34959.5
22	0.6	35458.53	35524.49
23	0.5	35029.86	34943
24	0.6	35495.85	35419.5
25	0.7	28673.84	28091.5
26	0.2	35409.03	35423
27	0.8	37318.77	37362

Table A5.1 data obtained from MicroCT imaging of tubes which first imaged by OPT

Appendix 6: values (Mean and Median) obtained from the fluorescent imaging

Samples	Amount of silver	Average	Median
1	0.4	2960.43472	3053.1
2	0.2	2398.38767	2425.35
3	0.1	2080.19	2085.0833
4	0	2004.40533	2003.61667
5(EtOH)	0.4	2659.8563	2775.5
6 dia	0.4	2595.98085	2692.23333

Table A6.1 data obtained from OPT imaging sample 1-6

Samples	Amount of silver	Average	Median
16	0.025	737.78995	737.466667
17	0.05	871.52225	873.916667
18	0.2	1068.07288	1120
19	0.3	1127.8644	1172.96667
20	0.4	1265.54467	1343.85
21	0.5	1217.00327	1283.88333
22	0.6	1327.497967	1425.4
23	0.5	1507.09345	1618.65
24	0.6	1434.0794	1548.96667
25	0.7	1560.45422	1689.86667
26	0.2	1140.34973	1179.5
27	0.8	1461.3865	1583.68333

Table A6.2 data obtained from OPT imaging sample 16-27

Appendix 7: Bright field images (1st, 200th, 400th frames) of samples 17, 25 ,27

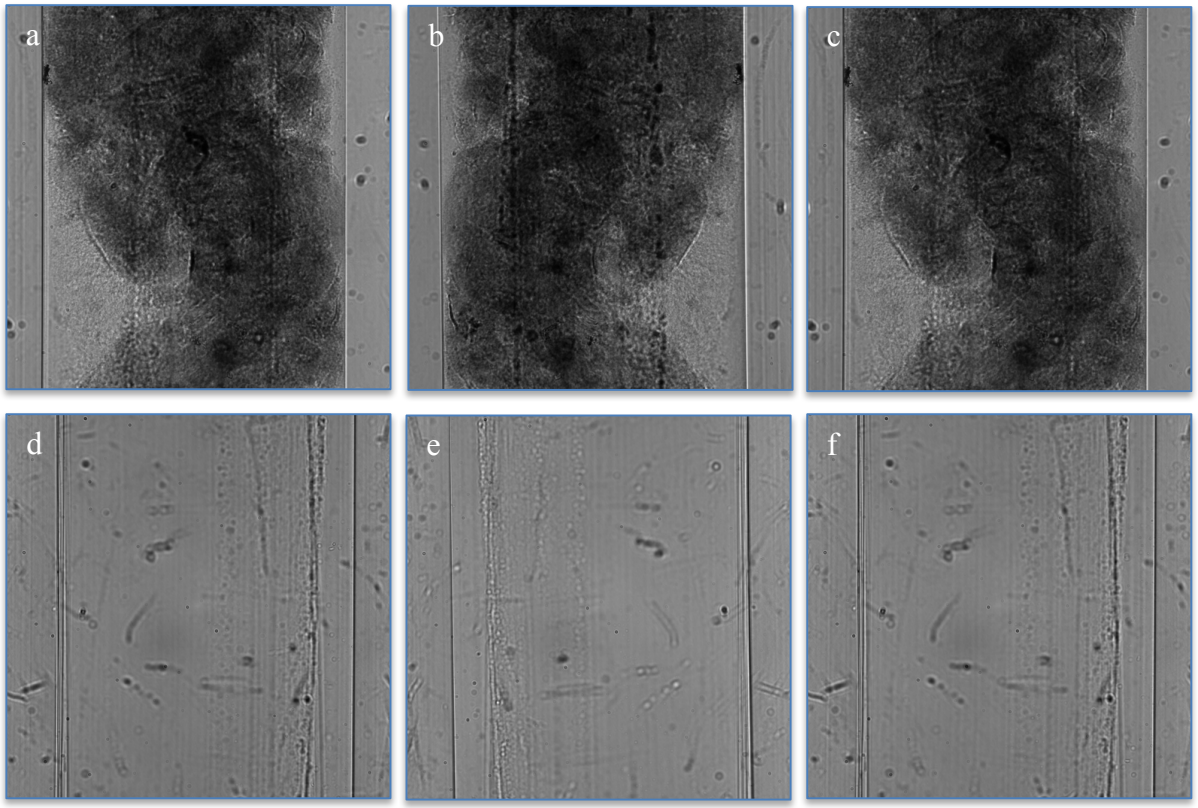

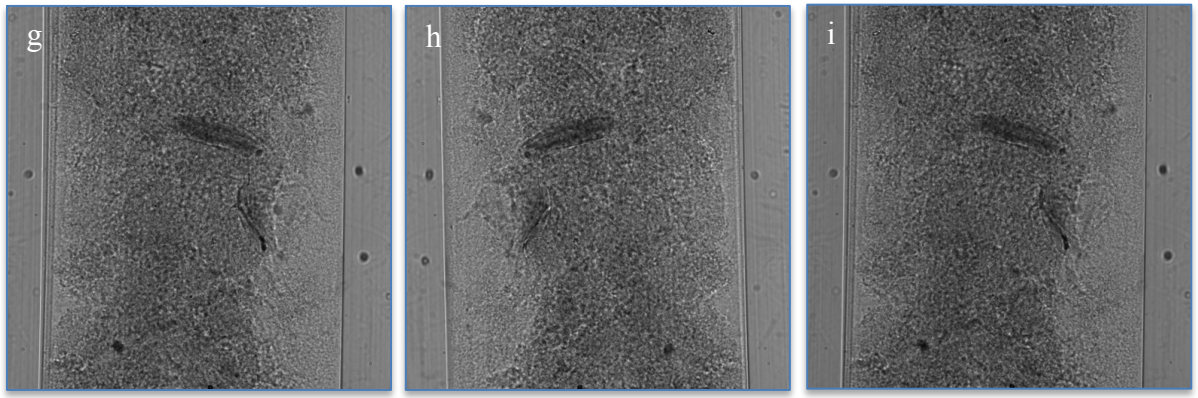

Figure A7.1 Bright field imaging of sample 17,25 and 26. a,b,c correspond to frames 1,200,400 of sample 17 Respectively. d,e,f correspond to frames 1,200,400 of sample 25 respectively. g, h,i correspond to frame 1, 200,400 of sample27, respectively.